

Supernova Remnants in the Magellanic Clouds V: The Complex Interior Structure of the N206 SNR

R. M. Williams, Y.-H. Chu, J. R. Dickel & R. A. Gruendl

University of Illinois at Urbana-Champaign, 1002 W. Green St., Urbana, IL 61801 USA

rosanina@astro.uiuc.edu, chu@astro.uiuc.edu, johnd@astro.uiuc.edu,
gruendl@astro.uiuc.edu

F. D. Seward

*Harvard-Smithsonian Center for Astrophysics, 60 Garden Street, MS 4, Cambridge, MA
02138 USA*

fds@cfa.harvard.edu

M. A. Guerrero¹

*Instituto de Astrofísica de Andalucía, Consejo Superior de Investigaciones Científicas
(CSIC), Apartado Correos 3004, E-18080 Granada, Spain*

mar@iaa.es

and

G. Hobbs

Australia Telescope National Facility, P.O. Box 76, Epping, NSW 1710, Australia

ghobbs@atnf.csiro.au

ABSTRACT

The N206 supernova remnant (SNR) in the Large Magellanic Cloud (LMC) has long been considered a prototypical “mixed morphology” SNR. Recent observations, however, have added a new twist to this familiar plot: an elongated, radially-oriented radio feature seen in projection against the SNR face. Utilizing the high resolution and sensitivity available with the *Hubble Space Telescope*, *Chandra*, and *XMM-Newton*, we have obtained optical emission-line images and spatially resolved X-ray spectral maps for this intriguing SNR. Our findings present the SNR itself as a remnant in the mid to late stages of its evolution.

X-ray emission associated with the radio “linear feature” strongly suggests it to be a pulsar-wind nebula (PWN). A small X-ray knot is discovered at the outer tip of this feature. The feature’s elongated morphology and the surrounding wedge-shaped X-ray enhancement strongly suggest a bow-shock PWN structure.

Subject headings: supernova remnants — ISM: individual (SNR B0532-71.0) — X-rays: ISM — Magellanic Clouds

1. Introduction

The supernova remnant (SNR) B 0532–71.0 lies to the north and east of the H II region LH α 120-N206¹ in the Large Magellanic Cloud (LMC). The SNR was first identified in radio by Mathewson & Clarke (1973), who referred to it simply as N206. Although this is more properly the name of the larger H II complex, for simplicity we shall use the same notation in the following discussion.

H α images of N206 obtained from the Magellanic Cloud Emission-Line Survey (Smith et al. 1999) show largely shell-like emission, with complex filamentary structure along the limb. Williams et al. (1999) noted that these features were in sharp contrast to the X-ray emission as observed by *ROSAT*, which shows the X-ray emission brightening toward the center of the remnant. The striking difference between X-ray and optical morphologies led the authors to categorize N206 as a “centrally brightened” SNR, and to suggest that it might undergo the same physical processes as “mixed morphology” SNRs (Rho & Petre 1998), which have centrally brightened X-ray emission and a radio shell.

Milne et al. (1980) studied N206 at 5 and 14.7 GHz, and found a spectral index α (as in $S \sim \nu^\alpha$) over the remnant of about -0.33 . This value is fairly flat for a SNR; it is on the borderline between the ranges for a pulsar wind nebula (PWN), for which spectral indices tend to be flatter than -0.4 , and for a typical shell-type remnant, for which spectral indices tend to be between -0.8 and -0.3 (Trushkin et al. 2000). Low resolution (several-arcminute scales) and interference from the nearby H II region made features in the SNR interior difficult to examine.

Of particular interest, therefore, are the observations by Klinger et al. (2002) of N206 at 3 and 6 cm wavelengths (8.0 and 4.8 GHz), using the Australia Telescope Compact Array (ATCA) with resolutions of $1''.8$ and $1''.1$ (HPBW), respectively. They saw emission over the

¹Catalogue number from Henize (1956)

face of the entire SNR, somewhat brightened toward the limb. The spectral index calculated from their findings and those of other radio observations was -0.20 ± 0.07 , in the normal range for filled-center SNRs. Klinger et al. (2002) also discerned a “peculiar linear feature” within the SNR: a narrow wedge of radio emission aligned in projection with the remnant’s center. A spectral index map of the SNR showed this feature to have a similar index to the rest of the remnant, ~ -0.2 . In the absence of high-resolution X-ray data, the authors could not isolate a point source, and therefore could only speculate that the feature was produced by “a low-mass star or compact object.” Using the “opening angle” of the linear feature to calculate the Mach number of the presumed object’s travel, and the length of the linear feature, the authors obtained an estimate for the SNR age of 23,000 yr.

2. Observations

2.1. X-ray Images and Spectroscopy

X-ray observations of N206 were made with both the *Chandra* and *XMM-Newton* observatories. *Chandra* observations used the Advanced CCD Imaging Spectrometer (ACIS), primarily the S3 back-illuminated chip. Datasets were sequence number 500327, observations 3848 (33.1 ks) and 4421 (32.5 ks). Data were reduced following procedures recommended by the Chandra X-ray Center (CXC) and analyzed using the CXC’s CIAO program and XSPEC. The two datasets were filtered for high-background times and poor event grades, resulting in a total “good time” interval of 65.6 ks. For each dataset, the $0''.5$ pixel randomizations were removed and the “subpixel resolution” technique² was applied, allowing us to more closely examine the structure on small spatial scales.

The filtered datasets were then merged, and spectral results extracted from the merged file. As spectral analysis required us to choose fairly wide regions for reasonable counting statistics, the “subpixel resolution” files were not used for this purpose. A background region was taken from an annulus surrounding the SNR, and the spectrum of this background region was scaled and subtracted from the source spectra. Individual spectra for regions of interest selected from radio and X-ray images, and the corresponding primary and auxiliary response files, were extracted with the CIAO `psextract` script and analyzed in XSPEC. Spectra were rebinned by spectral energy to achieve a signal-to-noise ratio of 4 in each bin.

²This technique, developed by Koji Mori, allows users to improve the spatial resolution by $\sim 10\%$ without decreasing the overall count rates. Documentation at http://cxc.harvard.edu/contsoft/software/subpixel_resolution.1.4.html

We received the pipeline-processed *XMM-Newton* data from the Science Operations Centre (SOC). Observations were made simultaneously with multiple *XMM-Newton* instruments; in this paper we will concentrate on the European Photon Imaging Camera (EPIC) MOS and pn detectors. The EPIC-MOS data were taken over two intervals, in 2001 November (Observation ID 089210901, 41.4 ks) and 2001 December (0089210101, 14.5 ks). The latter observation also included an EPIC-pn exposure (12.0 ks). Initial reduction and analysis were carried out using the Science Analysis Software (SAS) package provided by the SOC, with subsequent spectral analysis in XSPEC.

The data were filtered to remove high background times or poor event grades, reducing the total “good” dataset time to 24.2 ks for the first observation (EPIC-MOS only) and 12.0 ks for the second observation (EPIC-MOS and EPIC-pn). Images and spectra were then extracted from the filtered event files. Background regions immediately surrounding the SNR but free of point sources were used to produce background spectra, which were then scaled and subtracted from the source spectra. Joint spectral fits were performed with the data from the two EPIC-MOS observations.

2.2. Optical Emission-line Images and Spectroscopy

Images of N206 were obtained with the *Hubble Space Telescope* using the Wide Field Planetary Camera 2 (WFPC2) with the F656N ($H\alpha$), F673N ($[S\ II] \lambda\lambda\ 6347, 6371\ \text{\AA}$) and F502N ($[O\ III] \lambda\lambda\ 5007\ \text{\AA}$) filters. The southwestern side of the SNR was observed in $H\alpha$ ($3\times 800\ \text{s}$), $[S\ II]$ ($3\times 800\ \text{s}$) and $[O\ III]$ ($6\times 800\ \text{s}$), all at the same pointing and position angle, but the northeastern side of the SNR was observed only in $H\alpha$ ($3\times 800\ \text{s}$). The data were reduced using the IRAF³ program and STSDAS package. Multiple exposures were combined to remove cosmic-ray events, and the resulting files were bias-subtracted. The images were divided by exposure times to produce count-rate maps, which were then multiplied by the PHOTFLAM parameter (provided in the image header) to convert these to flux-density maps. We used the SYNPHOT task to determine widths for each filter, and multiplied the flux-density maps by the filter widths to produce flux maps. The files for the WFC and PC were then mosaicked together for the final images. Images for $[S\ II]$ and $H\alpha$ were clipped at 3σ of sky background to reduce noise, and then divided to produce a calibrated $[S\ II]/H\alpha$ ratio map.

High-dispersion spectra of N206 were obtained with the echelle spectrograph on the 4 m telescope at Cerro Tololo Inter-American Observatory (CTIO) from two observing runs,

³Image Reduction Analysis Facility, maintained by NOAO

2000 December 6 and 2004 January 14. Both runs used the 79 line mm^{-1} echelle grating in the single-order, long-slit observing configuration, in which a flat mirror replaced a cross disperser and a post-slit $\text{H}\alpha$ filter ($\lambda_c = 6563 \text{ \AA}$, $\Delta\lambda = 75 \text{ \AA}$) was inserted to isolate a single order. The red long focus camera and the 2000×2000 SITe2K#6 CCD were used to record data. The $24 \mu\text{m}$ pixel size corresponds to roughly 0.082 \AA along the dispersion and $0''.26$ perpendicular to the dispersion. Limited by the optics of the camera, the useful spatial coverage is $\sim 3'$. The spectral coverage is wide enough to include both the $\text{H}\alpha$ line and the flanking $[\text{N II}] \lambda\lambda 6548, 6583$ lines. A slit width of $250 \mu\text{m}$ ($1''.64$) was used and the resultant FWHM of the instrumental profile was $13.5 \pm 0.5 \text{ km s}^{-1}$. The spectral dispersion was calibrated by a Th-Ar lamp exposure taken in the beginning of the night, but the absolute wavelength was calibrated against the geocoronal $\text{H}\alpha$ line present in the nebular observations. The journal of echelle observations is given in Table 1.

2.3. Radio Pulsar Observations

We undertook new observations using the Parkes 64-m radio telescope at the Australia Telescope National Facility. We observed N206 for 12 hours on 2003 September 29 using the central beam of the 20-cm multibeam receiver at 1374 MHz on the Parkes telescope with the aim of detecting pulsed emission from a small X-ray source. Following the recent successful surveys for pulsars in radio nebulae at Parkes (Camilo et al. 2002a,b), we recorded total-power signals from 96 frequency channels which provide a bandwidth of 288 MHz for two polarizations every 1 ms. The sensitivity of the system was $\sim 20 \mu\text{Jy}$ which is a factor of ~ 2.5 more sensitive than an earlier, large-scale survey of the Large Magellanic Cloud (Fan 2002). Off-line processing was carried out to search for any dispersed, periodic signal using standard procedures with the SEEK software.⁴ No signal was detected.

3. Physical Structure of the SNR

The morphology of the SNR in the *XMM-Newton* and *Chandra* observations is complex, with particular structures revealing themselves variously under *XMM-Newton*'s high sensitivity and *Chandra*'s high resolution. In both cases (Fig. 1) diffuse emission can be seen over the entire face of the remnant, all the way out to the rim; and a significant increase in X-ray emission appears toward the center. In the *XMM-Newton* EPIC-pn and EPIC-MOS observations there is an extension of this central emission that corresponds well to the po-

⁴Source code and documentation are available at <http://www.jb.man.ac.uk/~drl/seek>.

sition of the radio “linear feature”. This apparent correlation is confirmed by the *Chandra* observations, in which X-ray emission is clearly seen along the length of the linear feature, broadening in the same region of the “wedge” as in radio (Fig. 2).

An X-ray point source appears in the *Chandra* observation at $05^h32^m03^s$, $-71^\circ00'51''$. No counterpart to this source is found in the optical or radio data. A search of the SIMBAD database shows these coordinates to be within the error circle for *Einstein* source 2E 0532.6–7102 (McDowell 1994). In the absence of features indicating an association between this source and the SNR, we presume it to be a background source; possibly, given its hard X-ray emission, an active galactic nucleus. We will not include this source in the subsequent discussion.

The *Hubble Space Telescope* WFPC2 $H\alpha$ mosaic of N206 in Figure 3 shows the circular, limb-brightened structure of this SNR. An intricate array of loop-like filaments extends from the outermost limb well within the remnant. Toward the southwest of the SNR the $H\alpha$ emission becomes more prominent; this is unsurprising, as in this region the N206 SNR may overlap slightly with the larger N206 H II region.

The [O III] emission, as seen in Figure 4c, tends to the outer edges of the filaments. [O III] is a useful “tracer” of shock fronts, due to the relatively narrow range of temperatures and densities in which this emission dominates. Thus the tendency of the [O III] to lie in the limbward direction of the filaments implies a fairly regular expansion. There do not appear to be any counterparts in $H\alpha$ or [O III] to the linear feature seen in radio by Klinger et al. (2002). The $H\alpha$ and [S II] morphologies, shown in Figure 4a and b, are quite similar, including the filamentary structure, as is typical for cooled ($\sim 10^4$ K) post-shock gas.

3.1. Hot Gas in the SNR’s Interior

Spectral fits to the X-ray data from the various instruments (*Chandra* ACIS, *XMM-Newton* EPIC-MOS and EPIC-pn) show that the emission from the SNR is dominated by thermal emission; a number of thermal emission lines are visible (Fig. 5). We therefore utilized thermal plasma models to determine the plasma parameters. As it is uncertain whether the plasma has reached ionization equilibrium, we fit both a non-equilibrium ionization model (NEI; “pshock” in XSPEC) and a collisional-ionization equilibrium model (CIE; “MeKaL” in XSPEC)⁵. We selected the following regions for further analysis: (Region 1) one comprising

⁵Details and references for the pshock and MeKaL models can be found at <http://heasarc.gsfc.nasa.gov/docs/xanadu/xspec/manual/node39.html> and [node40.html](http://heasarc.gsfc.nasa.gov/docs/xanadu/xspec/manual/node40.html).

the entire SNR for comparison with other X-ray studies; (2) a region enclosing much of the SNR limb, which is expected to be dominated by emission from recently shocked gas; (3) a region enclosing the central X-ray brightening but excluding emission thought to be associated with the “linear feature”; (4) a region covering an apparent wedge-shaped X-ray brightening north and south of the “linear feature”, excluding a possible point source; (5) a region corresponding to the “linear feature” seen in radio; (6-8) three equal-area regions along this feature to examine possible changes over its length; (9) a small region surrounding a possible point source at one end of the “linear feature”; (10) a region covering emission immediately behind the possible point source, excluding a narrow area corresponding to the brightest radio emission from the “linear feature”; and (11) a region covering the aforementioned radio-bright linear feature. A list of the regions used for X-ray analysis is given in Table 2 and shown in Figure 6.

We chose two of these regions thought to include only thermal X-ray emission: “Outer Limb” (Region 2, Fig. 6b) and “Central” (Region 3, Fig. 6c). We compared the fits of simple thermal models to the data from each of the X-ray instruments used (Table 3). Best fits are obtained with sub-solar metal abundances, consistent with the ambient metal abundances in the LMC of about 30% solar (Russel & Dopita 1992). Fits to the absorption column density are reasonably consistent for regions with good statistics, giving $N_{\text{H}} = 3 \pm 1 \times 10^{21} \text{ cm}^{-2}$. Fits to the temperature differ by a factor of two depending on whether CIE or NEI is assumed; CIE fits have $kT = 0.23 \pm 0.01 \text{ keV}$ and NEI fits have $kT = 0.4 \pm 0.1 \text{ keV}$ (Table 3). The fits to the ionization parameter τ ($= nt$, where n is the hot gas density and t is the time since ionization) indicate that the hot gas deviates considerably from ionization equilibrium, with $\tau = 3 \pm 1 \times 10^{11} \text{ cm}^{-3} \text{ s}$. In general, the NEI model also provides a better statistical fit to the data. We will therefore refer primarily to the results of the NEI fits in the subsequent discussion.

3.1.1. Overall SNR Characteristics

In order to facilitate comparison of our X-ray results with other X-ray studies at lower resolution, we include the “Whole SNR” region (Region 1 in Table 2, Fig. 6a), which includes all X-ray emission from the remnant, including that from the area of the “linear feature”. These fits (Table 4) largely fall within the range described above for the “Outer Limb” and “Central” regions, indicating that the SNR’s emission is dominated by other sources of emission than that of the “linear feature.” While an additional power-law component with a normalization of one-third that of the thermal plasma component slightly improves the fit, this improvement is not significant. The NEI fit yields an absorbed flux of $7 \pm 2 \times 10^{-13} \text{ erg}$

$\text{cm}^{-2} \text{ s}^{-1}$, an unabsorbed flux of $4 \pm 2 \times 10^{-12} \text{ erg cm}^{-2} \text{ s}^{-1}$, and a luminosity of $8 \pm 4 \times 10^{35} \text{ erg s}^{-1}$, all over the 0.3–8.0 keV range.

The normalization of the NEI model fits to X-ray data can be used to calculate the rms electron density (n_e) of the hot gas within the SNR. We assume the remnant to be roughly spherical, with a radius of 21 pc, at a distance of 50 kpc. We further assume that the gas is composed of fully ionized hydrogen and helium ($n_e \sim 1.2n_{\text{H}}$). Then, using the normalization from NEI fits to the Chandra ACIS data for the “Whole SNR” region (Table 4) we find a density in the hot gas of $n_e = 0.24 \pm 0.05 f_{\text{hot}}^{-1/2} \text{ cm}^{-3}$. Using the “Outer” and “Central” regions (Table 5-6), which do not include emission from the area around the “linear feature,” for this calculation gives a very similar density of $n_e = 0.23 \pm 0.09 f_{\text{hot}}^{-1/2} \text{ cm}^{-3}$. The parameter f_{hot} is a volume filling factor for the hot gas. If we assume $f_{\text{hot}}=1$, to reflect the centrally filled X-ray morphology of the remnant, the hot gas density is $n_e = 0.24 \pm 0.09 \text{ cm}^{-3}$; if the gas only partially fills this volume, the density will rise in inverse proportion to the square root of this filling factor.

From this derived density of the X-ray emitting material, we obtain a mass of $5.3 \pm 0.2 \times 10^{35} f_{\text{hot}}^{1/2} \text{ g}$, or $270 \pm 10 f_{\text{hot}}^{1/2} M_{\odot}$. Presuming that the hot gas fills the entire remnant ($f_{\text{hot}}=1$), this mass is greater than that expected from SN ejecta alone, emphasizing that N206 is an older SNR whose emission is dominated by swept-up material from the surroundings; and supports the LMC-like abundances found from the spectral fit. Using the temperature and density from spectral fits to the X-ray data, we find a thermal pressure, $P_{\text{th}} = nkT$, of $3.3 \pm 0.4 \times 10^{-10} f_{\text{hot}}^{-1/2} \text{ dyne cm}^{-2}$ in the hot gas. As the analysis in §3.2 will show, this is significantly greater than the thermal pressure we find for the cool shell. We can also calculate the thermal energy in this gas, $E_{\text{th}} = 1.5nfVkT$. This gives a thermal energy of $6 \pm 1 \times 10^{50} f_{\text{hot}}^{1/2} \text{ erg}$ for the hot gas. Finally, we can estimate the shock velocity under the (somewhat dubious) assumption that the bulk of the X-ray emission is being generated at the current shock front, using $kT = (3/16)\mu v_{\text{shock}}^2$, with the reduced mass $\mu = 0.61$ (for He:H = 1:10). If we presume the newly shocked gas to be at 0.45 keV, we find that such a temperature would result from a shock speed of 620 km s^{-1} , implying an overall expansion velocity of 470 km s^{-1} . For simplicity, we have assumed in the above calculations that the ions have equilibrated with the electrons; although this assumption may well not be valid, it provides us with at least initial estimates. The derived energy and pressure are similar to those for other SNRs in the adiabatic stage of evolution.

3.1.2. *Specific Hot Gas Features*

N206 is clearly more complex than the simple shell approximated above. It features an increase in surface brightness toward the remnant center, a “wedge” of emission appearing to surround the “linear feature”, and the feature itself, terminating in a possible compact source. The properties of these features will be discussed in more detail in §4.

The central brightening on the SNR is quite puzzling. The spectrum of this region (Table 6) appears similar to that for the limb of the remnant, with slightly higher abundances, particularly oxygen. There is no evidence for a strong power-law component in this region; fits with such a component require it to be normalized to a small fraction of the thermal component’s emissivity.

Toward the eastern side of the remnant, surrounding the “linear feature,” the X-rays show a slightly brighter broad “wedge” of emission (Region 4 in Table 2, Fig. 6c). Fits to the spectrum of this region (Table 7; this spectrum does not include contributions near the “compact source”) suggest a markedly higher plasma temperature than elsewhere in the SNR. While a nonthermal contribution might artificially skew a thermal model fit toward higher temperatures, fits which included nonthermal emission over a tenth of the thermal emissivity could be statistically ruled out at the 90% level.

We also examined a region covering the area of the “linear feature”, as seen from radio images (Region 5 in Table 2, Fig. 6d). We defined a hardness ratio ($H-S/H+S$) such that $S=0.3-1.0$ keV and $H=1.0-8.0$ keV (Table 2). Using these hardness ratios to compare this region to others throughout the SNR, we find that, while the contribution of soft-X-rays still dominates, the proportion of hard X-rays in this region is greater than elsewhere in the SNR. This increase in the hardness ratio is consistent with the combination of thermal emission from the SNR and emission from a harder source, as for example the small-diameter bright source at the tip of this region. While a localized increase in temperature could also explain this hardening, it would be quite coincidental that this increase appears only in this portion of the SNR that also shows the small-diameter X-ray source and elongated radio feature (Fig. 1c-e).

We performed spectral fits to data from Region 5, though we note that these fits are somewhat limited by the relatively low number of counts. We find that either a thermal plasma model or a power-law model can provide a statistically adequate fit to this source (Table 8). The “best” fit arises from a combination of nonequilibrium thermal plasma and power-law models, providing roughly equal contributions to the spectrum. Although the improvement in the fit is not statistically significant, such a combination is consistent with the scenario inferred from the hardness ratios. To examine the detailed properties of the

“linear feature”, we used the *Chandra* ACIS data to analyze emission from smaller segments along that feature (Regions 6-8 in Table 2, Fig. 6e). These fits, summarized in Table 9, should be considered as preliminary estimates only.

3.2. The Cool Shell of the SNR

Figure 4d shows an [S II]/H α ratio map of the southwestern side of N206. [S II]/H α ratios range from 0.7 to 1.2 across the SNR, typical for shocked gas, with an average value of 0.9. This is initially somewhat surprising, as it indicates that there has not been much ionization of material from the nearby OB association. However, H I maps of the vicinity show an H I shell, with the N206 H II region largely situated within the central cavity, so that the H I shell walls probably block most of the ionizing radiation before it can reach the SNR (Dunne, Chu & Stavelly-Smith 2005).

We measured the average H α surface brightness of filaments in the flux-calibrated WFPC2 image of N206 to be $(0.8-1.8)\times 10^{-17}$ erg cm $^{-2}$ s $^{-1}$ pix $^{-1}$, or $(0.8-1.8)\times 10^{-15}$ erg s $^{-1}$ cm $^{-2}$ arcsec $^{-2}$. Assuming a cool shell temperature of 10^4 K, this surface brightness implies an optical emission measure of 680 ± 260 pc cm $^{-6}$. We presumed the average filament thickness along the line of sight ($20'' - 30''$) to be equal to its width perpendicular to the line of sight, and used this as a representative number for the path length \mathcal{L} through the warm ionized gas. Using this \mathcal{L} , we calculate an rms electron density in the shell of about 10 ± 4 cm $^{-3}$. If we presume the SNR to be in the adiabatic “point-blast” stage of expansion (Sedov 1959), and the cool shell to be representative of the ambient ISM, we would expect the ambient ISM density to be roughly one-quarter of that in the shell, or about 3 ± 1 cm $^{-3}$.

The optical echelle data (Fig. 7) show several lines in the H α spectral region, including the narrow geocoronal H α (6562.85 Å) and telluric OH 6-1 P2(3.5) 6568.779 and 6-1 P1(4.5)e/f 6577.183/.386 lines (Osterbrock et al. 1996), as well as broader lines corresponding to Doppler-shifted nebular H α emission toward the SNR. The latter include both a velocity component constant along the slit, showing the systemic velocity of the SNR, and the characteristic bow-shaped pattern deviating from this systemic velocity, showing motions within the expanding gas.

In order to measure the systemic velocity, we extracted a velocity profile from a region $13''$ wide outside of the emission of the SNR expansion pattern. The profile showed two components, one of which was identified as the telluric OH line. The other component is the H α line with a measured Doppler shift of 241 ± 4 km s $^{-1}$; as the SNR expansion pattern appears to converge to this component, we take this as the systemic velocity for the N206

SNR. For comparison, we note that the nearest position to N206 in the H I maps of Rohlfs et al. (1984) shows velocity components at 240 ± 7 and 262 ± 26 km s⁻¹.

To characterize the expansion of the N206 SNR, we measure the velocity offsets (Δv) from the systemic velocity in both the blue and red directions. As the material at the forefront of the SNR expansion may be reasonably expected to show the highest velocity, we take the greatest of these velocity offsets to represent the overall expansion velocity of the remnant. The greatest offset in the blue direction (Δv_{blue}) is -202 ± 5 km s⁻¹, while the largest $\Delta v_{\text{red}} = +193\pm 5$ km s⁻¹. We therefore estimate the expansion velocity $v_{\text{exp}} = 202\pm 5$ km s⁻¹. Using this value for expansion, and assuming that the SNR is in the Sedov phase, we would expect the shock velocity $v_{\text{shock}} = 4/3 v_{\text{exp}} = 270\pm 5$ km s⁻¹. It should be noted that the errors given here are only the random errors of the measurements.

It is possible that some of the optically emitting material is too faint for detection in these observations. If the highest-velocity material is undetected, the actual expansion velocity may be higher than our estimate. For example, Chu & Kennicutt (1988) found a higher expansion rate of 250 km s⁻¹; the discrepancy may be due to the difficulty of discerning motions in the faint outer material. To an extent, this may also apply to the large discrepancy between the shock velocity calculated from the temperature of the hot gas in §3.1.1, and that measured from the warm ionized gas. More likely, however, this discrepancy is due to two factors. (1) The X-ray temperature may not be a reliable representation of the newly shocked gas, particularly given its large deviation from a limb-brightened shell morphology. (2) We expect the X-ray emission to arise from areas where the shock front is moving through diffuse gas, while the optical emission is expected to be generated where the shock is moving through higher density gas, as seen in the relative densities of the hot gas to the warm ionized gas. Thus, we expect that the shock within the optically-emitting clumps has been somewhat slowed by its progress through this denser material. The overall expansion velocity from the blast wave is probably intermediate between the measured optical expansion of 202 km s⁻¹ and the calculated expansion from X-ray temperatures of 470 km s⁻¹.

Using the shell electron density of $n=10$ cm⁻³ calculated above, and presuming $n_{\text{He}}/n_{\text{H}} = 0.1$ and singly ionized He ($n_e = 1.1n_{\text{H}}$), we can infer the mass of gas in the shell according to $M = nm_{\text{H}}V_{\text{shell}}$, where V_{shell} is the shell volume. From the filamentary structure at the edge of the shell, we measure an average shell thickness of about $1''.1\pm 0''.5$ (0.27 ± 0.13 pc at a distance of ~ 50 kpc to the LMC). If we assume a simple spherical shell of this thickness, we calculate a shell mass of $9\pm 6 \times 10^{35}$ g, or $460\pm 300 M_{\odot}$. This is almost certainly an underestimate, as the filamentary structure shows a much greater extent of cool gas than such a simplistic scenario. If instead we presume the cool gas occupies a volume filling factor

of as much as 0.1, we obtain a mass estimate of $2.4 \pm 1.7 \times 10^{36}$ g, or $1200 \pm 800 M_{\odot}$.

Using these as low- and high-end estimates of the mass range, and the expansion velocity above, we calculate the kinetic energy in the cool shell, $0.5M_{\text{shell}}v_{\text{exp}}^2$, to find values of $2 \pm 1 \times 10^{50}$ erg and $5 \pm 3 \times 10^{50}$ erg, respectively. One can also use the density calculated above to calculate the thermal pressure in the shell, $P = nkT$, where k is the Boltzmann constant and T is the temperature, presumed here to be 10^4 K. This equation gives a pressure of $3 \pm 1 \times 10^{-11}$ dyne cm^{-2} . Again, these values for kinetic energy and shell pressure are typical for middle-aged SNRs. The physical characteristics of the N206 SNR are summarized in Table 10.

4. Specific Radio and X-ray Features

The high spatial resolution of *Chandra's* ACIS allows us to examine specific regions in more detail. We have isolated three features that appear to be of particular interest: X-ray emission associated with the radio-identified “linear feature;” the X-ray knot and surrounding emission which coincides with the very tip of that linear feature; and the region of enhanced X-ray surface brightness toward the center of the SNR. Below, we describe each of these features individually and then discuss the possible origins for these features.

4.1. Central Emission

The interior X-ray emission is brightest from an irregular region extending N–S for half the diameter of the remnant. This central emission is clearly dominated by thermal X-rays, with prominent line features including the blends of He-like lines of Mg and Si. The emission is largely soft (< 2 keV) and thermal plasma fits to data from this region give parameters for N_{H} and kT similar to those found for the SNR as a whole. However, there does appear to be some difference in abundance distributions between the central area and the outer regions of the SNR (excluding emission associated with the “linear feature”). The oxygen lines in the central region are more prominent, with respect to the iron blends (Fe L), than in other regions of the SNR (Table 6). These differences should be treated with caution, as there are large uncertainties in the abundance determinations; however, the difference in oxygen abundance between the two regions within the SNR is significant when compared to the 90% error ranges for this quantity. If the central emission is due to “fossil radiation,” i.e. gas that was shock-heated during earlier phases of the SNR expansion, we would expect that this gas would have a higher proportion of ejecta to swept-up matter than the more

recently-shocked gas, and therefore that the higher oxygen abundance reflects the presence of oxygen-rich ejecta, as seen in the much younger mixed-morphology SNR 0103-72 in the SMC (Park et al. 2003). The presence of O-rich material cannot be confirmed from *Hubble Space Telescope* [O III] maps. This probably reflects the fact that the X-ray emission which shows the oxygen excess is primarily from the hot central cavity, where the temperatures are too high and the densities too low for [O III] to show up.

It is worth noting that in addition to the similar oxygen-rich and mixed-morphology SNR 0103-72 (Park et al. 2003), the oxygen-rich SNR N132D shows, likewise, a higher ratio of oxygen (O^{7+}) to other elements in the remnant interior than at the bright rim (Behar et al. 2001). Nucleosynthesis models indicate that a high oxygen abundance within a SNR’s ejecta is the result of a Type II SN (e.g., Tsujimoto et al 1995). The examples of “mixed-morphology” SNRs which show signs of enhanced oxygen abundances, therefore, may imply that the “mixed-morphology” SNRs are likely to have originated from Type II SNe.

As with other mixed-morphology SNRs (Rho & Petre 1998), the expanding shock of N206 has slowed to the point where bright X-rays from the limb do not dominate the overall emission from the remnant. Thus, it is reasonable to think that N206 follows the typical pattern for mixed-morphology SNRs, wherein the central emission is dominated by fossil radiation from earlier large-scale shock heating during the SNR’s evolution.

4.2. Linear Feature

An elliptical region (65" E–W \times 21" N–S) surrounding the “linear feature” in radio was selected from the 6 cm radio image (Klinger et al. 2002), and was used to extract spectra from the corresponding X-ray data (Region 5). Comparison of the hardness ratio for this region to those elsewhere in the SNR, as discussed in §3.1.2, suggests the presence of a hard component in addition to the soft emission seen throughout N206. A combined NEI and power-law model with $kT = 0.4 \pm 0.2$ and $\Gamma = 2.2 \pm 0.2$ provided the best fit. Fits to these spectra are summarized in Table 8. (Note that the value of τ obtained for this fit would indicate a plasma in collisional ionization equilibrium; we retain the NEI model, however, for consistency in intercomparison with the other fits.) Using these fitted values, we obtained an absorbed X-ray flux of $4 \pm 1 \times 10^{-14}$ erg cm $^{-2}$ s $^{-1}$ over the 0.3–8.0 keV range, which corresponds to an unabsorbed flux of 1×10^{-13} erg cm $^{-2}$ s $^{-1}$. At the LMC distance of 50 kpc, this gives a luminosity of 3×10^{34} erg s $^{-1}$ over this energy range.

To further examine the nature of this linear feature, a series of three equal-area regions (20" \times 15") E–W along the feature were identified in *Chandra* images for further spectral

examination (Regions 6-8 in Table 2). Comparison of the hardness ratios defined above for regions 6-8 shows a pronounced shift from regions dominated by high-energy photons to those dominated by low-energy photons.

We also performed spectral fits for these regions (Table 9). It should be stressed that, due to the low numbers of counts, these spectral fits are quite uncertain. Cited values of χ_{red}^2 are low due to the large error bars for the spectral bins; however, further binning was deemed undesirable due to the loss of remaining spectral information. However, as with the hardness ratios discussed above, the fits illustrate the shift from harder to softer emission along the feature.

In order to see whether the relative fluxes of thermal to nonthermal emission would change substantially as one moved from the remnant center toward the X-ray bright knot at the east end of the linear feature, we adopted a dual approach to these spectral fits. Initially, we fit a two-component (power-law and NEI) model jointly to all three regions, and determined the flux in each component for each region. As an alternate approach, we fit the power-law component to the high-energy end of the spectrum only (>2 keV) and fixed those parameters, then fit the joint model to the low-energy end of the spectrum. Again, the flux in each component was determined. The results, summarized in Table 11, indicate that the X-ray emission along the linear feature is more strongly dominated by nonthermal emission the further one moves eastward (closer to the knot) along the feature, and dies off on the west side. While this result is largely qualitative, given the errors, we argue that the increase in “hard” emission toward the knot is most likely to result from a nonthermal source.

The nonthermal spectra of the X-ray emission and radio emission in the “linear feature” imply the presence of a pulsar-wind nebula (PWN). The most likely source for nonthermal X-rays within a SNR is synchrotron radiation. While nonthermal X-ray emission may occasionally be generated by a fast SNR shock at the outer limb of a SNR, both the relatively slow expansion of this SNR and the shape of the emitting region of the nonthermal emission, i.e. over a small spatial segment perpendicular to the shell, argue against this scenario. Likewise, it seems unlikely that the motion of a compact source would be sufficient to produce a bow shock capable of generating significant synchrotron X-rays. The most plausible explanation, then, is that the acceleration of particles by a “hidden” pulsar is the source of the nonthermal emission (in both radio and X-rays) seen in the linear feature.

The westward decrease in the ratio of nonthermal to thermal X-ray flux along the linear feature suggests that it is a PWN generated by an eastward moving pulsar. The lifetime of the high-energy particles generated in a PWN is comparatively short; the radio-emitting particles persist and so trail farther behind the X-ray extent. The radio pulsar observations were unable to find any periodicity greater than 2 ms to the radio signal from the area of

the “linear feature”. It is by no means uncommon for a PWN to be detected in radio and X-rays without a radio point-source counterpart; for example, N157B, also in the LMC, was deduced to have a PWN long before the X-ray pulsar was discovered, and a radio counterpart for that pulsar has yet to be found (Wang et al. 2001).

Another possibility that must be considered, of course, is that these features are associated with a background source rather than the SNR. Klinger et al. (2002) discuss this scenario, but conclude that this is unlikely. The presence of extended nonthermal X-ray emission provides an additional reason to believe the feature is not a background source, as such a feature would be highly unusual in a background galaxy.

If we accept the premise that the “linear feature” is a PWN, we may anticipate that in part, the morphology of the PWN is created by a bow-shock structure. The dynamics of a rapidly moving pulsar and evolving SNR lead to the prediction of the formation of a bow shock when the SNR expansion speed has decelerated sufficiently for the pulsar’s motion relative to the shocked SNR material to become supersonic (e.g. van der Swaluw et al. 1998). At this point the PWN is deformed, leading to a substantial offset between the pulsar and the center of the PWN; this is certainly consistent with the observed bright knot at the outer tip of the “linear feature” presumptive PWN.

Numerical simulations predict that for a remnant in the Sedov stage, this should occur when the distance traveled by the pulsar from the center of the SNR, R_{PSR} , approaches the SNR radius R_{SNR} according to $R_{\text{PSR}}/R_{\text{SNR}} \gtrsim 0.677$ (van der Swaluw 2004; van der Swaluw et al. 1998). Presuming that the geometric center of the SNR shell accurately represents the site of the SN, the current position of the small-diameter X-ray source is such that the transverse component of R_{PSR} is $0.85 R_{\text{SNR}}$, well over the point for bow shock formation. If the direction of pulsar motion is not perpendicular to the line of sight, R_{PSR} increases accordingly. These findings are in general accord with those of Klinger et al. (2002), and their assumptions in their estimation of the pulsar velocity and age.

The fact that emission from the “linear feature” in X-ray and radio does not dominate the overall emission from the remnant presents an additional question. Its spectral index would place it among the most flat radio SNR shells, although overlapping (within the error bars) with remnants such as IC443 (Kawasaki et al. 2002). It is difficult to see why the SNR as a whole should show a radio index typical of filled-center remnants (Klinger et al. 2002) if the putative PWN is largely confined to this feature. However, the radio emission from N206 is faint compared to that from other SNRs, and therefore the uncertainties in the spectral index determination are considerable. In addition, residual emission from the N206 H II region may contaminate the radio emission, adding additional uncertainty.

4.3. Evidence for a Compact Source

In the *Chandra* images, a distinct knot of X-ray emission appears to the far eastward end of the linear feature, near the SNR limb. To investigate whether this knot is consistent with an unresolved source, we generated a point source of comparable X-ray flux using the MARX simulator, and compared the profile of this simulated source to that of the knot. We conclude that the knot is a small diffuse region of dimension $2''$. This can also be seen by comparison with the appearance of the moderately bright point source $\sim 50''$ SW of the knot (identified above with 2E 0532.6-7102). If a point source is embedded within the knot, only $\leq 50\%$ of the counts from the knot could be due to that point source.

We extracted counts within a $2''$ radius of the knot from the merged *Chandra* ACIS events file (Region 9 in Table 2, Fig. 6e), obtaining a count rate after background subtraction of 7.9×10^{-4} ct s $^{-1}$, or 52 counts over the 65.6 ks exposure time, an insufficient quantity to obtain a meaningful spectrum. Fig. 1, however, shows that the knot shows noticeably harder emission than that from the surrounding SNR. Once again using the hardness ratio defined above, (Table 2), we find a hardness ratio of 0.5 for the knot, in contrast to hardness ratios of -0.45 and -0.58 for the “outer” (Region 2; SNR limb excluding the putative PWN) and “central” (Region 3) areas.

To obtain a first-order estimate of spectral properties for this knot, we fixed N_{H} (and abundances, for the thermal case) to the values determined by fits to the X-ray emission from the rest of the SNR. The data are consistent with a thermal plasma model with temperatures > 1 keV, or a power-law model with a spectral index Γ between 2 and 3. Using a power-law model with $\Gamma = 2.4$, we obtain an estimate for the absorbed flux of 6×10^{-15} erg cm $^{-2}$ s $^{-1}$, an unabsorbed flux of 1×10^{-14} erg cm $^{-2}$ s $^{-1}$, and a luminosity of 3×10^{33} erg s $^{-1}$ at the LMC distance, all over the 0.3-8.0 keV energy range. The maximum luminosity for an embedded point source is therefore $\sim 1.5 \times 10^{33}$ erg s $^{-1}$ over this range.

An elliptical region ($5'' \times 8''$) immediately west of the knot, along the linear feature, yielded a count rate of 1.4×10^{-3} ct s $^{-1}$. This region has a very similar spectrum to that from the knot, suggesting that the spectrum determined from the knot is dominated by emission from its immediate surroundings. Combining the spectra from these two regions allowed us to increase the signal-to-noise ratio for a slightly better spectral fit. While these fits would still not allow us to rule out a thermal plasma interpretation at 90% confidence, they confirm that a relatively high temperature $kT > 1$ keV, is required. More plausible is a power-law fit, with $\Gamma = 2 \pm 1$, roughly consistent with that measured from the “linear feature” as a whole. While fits to smaller regions along the linear feature suggest a possible spatial variation in the power-law spectral index, the sensitivity of the X-ray observations is insufficient to make this determination at a statistically significant level.

A brief analysis of the X-ray power spectrum shows no evidence for periodic emission from an embedded pulsar. However, the timing resolution of these observations, 3.2 seconds, would not be sufficient to detect the pulsations from a typical pulsar. In addition, the estimated maximum of 25 counts from a point source is insufficient to determine a period for its emission, even if the timing resolution were available.

4.4. Possible Bow Shock

Proceeding westward from the knot, X-ray emission associated with the “linear feature” broadens into a wedge of brighter X-ray emission which then appears to merge with the central emission. Faint emission connects this patch to the compact knot close to the eastern rim. We interpret this connection as a “bow shock,” clear in the south and barely discernable in the north. This bow shock merges with the radio “linear feature” close to the knot. A bow shock in front of a hypothetical moving pulsar might re-heat the material through which it moves, leaving a trail of “fossil radiation” back to the remnant center and merging there with fossil radiation from much earlier fast-moving shocks.

One approach to these features would be to consider much of the X-ray emission between the bright linear feature and the central region as the actual boundary of the bow-shocked gas. In this case we would have a much larger opening angle for this structure than that found by Klinger et al. (2002). Using the X-ray opening angle of about $57^\circ \pm 5^\circ$ (1.0 ± 0.1 rad) we obtain a Mach number $\mathcal{M} = \sin(\theta/2)^{-1} = 2.1 \pm 0.5$. This is considerably lower than than the $\mathcal{M} = 9$ value of Klinger et al. (2002), and closer to the theoretical value for a pulsar moving through a SNR interior ($\mathcal{M} \approx 3.1$, van der Swaluw et al. 1998).

We can calculate the sound speed of the hot gas within the SNR according to

$$c_s = \left(\frac{\gamma k T_e}{\mu m_H} \right)^{\frac{1}{2}}$$

where γ is the adiabatic index, here taken as $5/3$; k is Boltzmann’s constant; T_e is the electron temperature; μ is the reduced mass; and m_H is the hydrogen particle mass. Presuming the reduced mass $\mu = 0.61$, and using the temperature found above, we obtain a sound speed in the hot gas of 230 ± 110 km s⁻¹. According to $\mathcal{M} = u/c_s$, where u is the motion of the pulsar relative to the SNR material, this gives a mean relative motion of $u = 480 \pm 240$ km s⁻¹.

If the pulsar is, as it appears, moving radially outward from the SNR center, we can presume its motion to be parallel to that of the expanding SNR material around the pulsar.

In order to obtain a mean relative velocity of $u=480 \text{ km s}^{-1}$ with material moving at the expansion velocity $v_{\text{exp}} = 202 \text{ km s}^{-1}$ (slow-expansion case), we would require the pulsar to be moving at a speed of roughly 680 km s^{-1} with respect to the SNR center. If instead we use the X-ray derived expansion speed of $v_{\text{exp}} = 470 \text{ km s}^{-1}$ (fast-expansion case), the pulsar must be moving with a speed of $\sim 950 \text{ km s}^{-1}$ with respect to the SNR center. If the motion is entirely perpendicular to the line of sight, and the pulsar began at the geometric center of the SNR, it would have taken the pulsar about 28,000 yr to reach its current transverse distance of 19.4 pc in the slow-expansion case, and 20,000 yr in the fast-expansion case. These can, of course, be affected by the viewing angle; but if we assume the pulsar to be interacting with the SNR interior, its maximum distance of travel is the SNR radius of 21 pc (at a 67° angle to the line of sight), which puts its time of travel at 30,000 yr in the slow-expansion case and 22,000 yr in the fast-expansion case.

In our suggested picture, the bow-shocked gas is primarily thermal, representing material within the SNR that is shocked to higher temperatures by the encounter with the bow shock. Presumably, the nonthermal X-ray emission is associated with the elongated PWN, as would be the radio emission. Thus we would expect a broad outer “cone” of thermal (shocked SNR material) emission, with an interior “cone” of nonthermal (shocked PWN) emission. Such a scenario is in accord with hydrodynamic models of bow-shock PWN, in which “the Mach cone should manifest itself only in the outer bow shock” (Gaensler et al. 2004, and references therein). The shocked PWN material forms a trail of synchrotron emitting particles opposite the direction of pulsar motion, creating a “cometary” or “linear” morphology.

To examine this picture for consistency with the data, we fit a simple thermal plasma plus power-law model combination to data from two regions within the linear feature: the thin “trail” region, corresponding to the narrow location of the brightest radio feature (Region 11 in Table 2, Fig. 6f), and the “bow” region, comprised of emission around the linear feature excluding the aforementioned “trail” (Region 10, Fig. 6f). Both regions excluded emission within $6''$ of the presumed pulsar. The best-fit model combination gave thermal and power-law parameters similar to those given in previous sections ($N_H \sim 2.6 \times 10^{21} \text{ cm}^{-2}$, $T \sim 0.26 \text{ keV}$, $\Gamma \sim 2.3$). Calculating the fraction of the total flux for each model component, we find that the “trail” region shows 96% nonthermal flux and only 4% due to thermal plasma, while the “bow” region shows 49% thermal flux and 51% nonthermal flux. Errors on these flux ratios, based on the differences in flux due to uncertainties in the fitted parameters at the 90% confidence level, are of order 10%.

Alternately, it is possible that some of the X-ray brightening we consider to be associated with the radio “linear feature” (excluding the X-ray knot) is in fact only a surface brightness fluctuation, and does not accurately represent the “Mach cone” of the presumptive moving

pulsar. If the “Mach cone” is more tightly confined than our X-ray based estimate, the resulting Mach number may be somewhat higher, up to a value of about $\mathcal{M} = 4$ when one considers only the angular extent of the bright X-ray emission immediately surrounding the X-ray knot. While it is also possible that the emission from these features is due to the PWN alone, with no substantial bow-shock emission, the highly elongated morphology and off-center pulsar position argue strongly for the presence of a significant bow-shock contribution.

5. SNR age

The ages of supernova remnants are notoriously ill-characterized. We consider a number of different approaches to this age, in order to find the range of reasonable age estimates. From the fitted X-ray parameters, several estimates are possible. Combining the derived hot gas density with the fitted ionization parameter τ gives an upper limit age estimate of $\sim 40,000$ years for this remnant. However, an age this large would be difficult to reconcile with the fact that the hot gas in the SNR has apparently not yet reached ionization equilibrium. Lowering the filling factor shortens this age estimate significantly. A filling factor of 0.25, for instance, gives an age estimate of 23,000 yr, similar to the estimate based on the radio “linear feature” by Klinger et al. (2002).

We can also make another estimate from the Sedov relations, in which the relative fractions of thermal and kinetic energies to total energy are constant. Taking the theoretical relation of $E_{\text{th}} \approx 0.7E_0$, our estimate for thermal energy (for $f_{\text{hot}} = 1$) would yield an initial explosion energy E_0 of 8×10^{50} erg. Assuming the density behind the shock is a factor of 4 greater than that of the unshocked ISM, we obtain an ISM mass density ρ_0 of 1.2×10^{-25} g cm^{-3} . Then from the Sedov relation $R = 1.17(E_0/\rho_0)^{1/5}t^{2/5}$, we have an age of only 9,000 yr. If the X-ray filling factor is lower than 1, the age estimate will rise accordingly; $f_{\text{hot}} = 0.25$, for instance, gives an age of 17,000 yr. If we instead presume the overall ambient density to be represented by the current filaments of warm ionized gas, we obtain an ISM mass density of 5.3×10^{-24} g cm^{-3} . The Sedov relation then gives an age as high as 57,000 yr, demonstrating the critical role played by the ambient density assumption.

Using the the simple expansion relation $t = \eta R/v_{\text{exp}}$, and assuming Sedov expansion ($\eta=0.4$), we can calculate the age of the remnant based on the expansion velocity. The expansion velocity of 470 km s^{-1} derived from the X-ray temperature gives a remnant age of 17,000 yr. The expansion velocity obtained from optical echelle spectroscopy of 202 km s^{-1} , however, leads to a calculated age of 41,000 yr. Again, however, this must be considered an upper limit, as this value of v_{exp} is, as stated above, a lower limit to the blast-wave expansion.

We can try to narrow down these estimates by considering the consistency of the entire picture. Ages above $\sim 40,000$ yr are clearly ruled out by the ionization timescale of the X-ray gas and by the observed optical expansion. The value of 9000 yr from energetics arguments is highly dependent on the assumption of ambient density; a better lower limit might be that of 17,000 yr from the expansion velocity derived from the X-ray temperature. When we consider the estimates of pulsar motion (§4.4) we find further limitations: the minimum time for the pulsar to reach its current location is $\sim 20,000$ yr, while the maximum is $\sim 30,000$ yr.

If we choose a velocity intermediate between the X-ray and optically derived values (e.g., ~ 300 km s $^{-1}$) and a hot gas filling factor of 0.25, we can reconcile most of these numbers. The ionization timescale for the hot gas then gives an approximate age of 23,000 yr. Pulsar travel times give ages (depending on viewing angle) between 24,000 – 26,000 yr. Simple Sedov expansion at this velocity gives an age of 27,000 yr. While arguments from Sedov energetics would, for this same filling factor, give us a somewhat lower age of 17,000 yr, this estimate is highly dependent on the assumption used for ambient density, a very uncertain parameter. We therefore suggest the SNR’s age most likely falls in the range between 23,000 – 27,000 yr, with “hard” limits of 17,000 yr – 40,000 yr.

6. Integrated Picture

We have observed the SNR in N206 with high-resolution optical and X-ray instruments, and analyzed the results in concert with additional radio data and optical echelle spectra. We find it highly probable that N206 is the result of a Type II SN, due to its proximity to other massive-star phenomena, enhancement of oxygen abundances, and the presence of a probable compact object.

We use these data to calculate overall properties for the physical components of the SNR, and find these typical of a middle-aged SNR in the adiabatic stage. The remnant is over-pressured, and the bulk of the energy budget still resides in thermal energy from the hot interior. Evidently, therefore, the hot gas within the SNR still plays a significant role in the remnant’s development.

This remnant is particularly unusual for the very different characteristics it displays in different wavelength regimes. The optical morphology is limb-brightened and highly filamentary; the radio morphology is center-filled, with diffuse emission over the remnant’s face, but some SNR shell structure; and the X-ray morphology appears somewhat centrally brightened. The best categorization for this remnant appears to be that of “mixed-morphology” (Rho & Petre 1998), but the picture is complicated by the presence of radio and X-ray

emission near the “linear feature”.

We analyze the X-ray data for the area surrounding the “linear feature” seen in radio. We find a small, hard X-ray source located at the tip of the radio feature, with a surface brightness profile consistent with the presence of an embedded compact source. Emission from this source and its surroundings is nonthermal, with a power-law index similar to that seen in Crab-type objects. The ratio of nonthermal to thermal X-ray flux decreases with increasing distance from this source. We conclude that the most probable scenario for this feature is a pulsar moving at moderate velocity through the surrounding SNR. This creates a bow-shock structure in the direction of motion, deforms the surrounding PWN, and leaves behind a trail of synchrotron emission along the line of travel.

However, it would be difficult to attribute most, or even the majority, of the central X-ray emission to that linear feature. The X-ray emission from the central region is clearly dominated by thermal line emission, rather than nonthermal continuum. The lifetime of relativistic particles energetic enough to generate X-ray emission is not sufficient for those particles to be responsible for the central X-rays, as indicated by the fact that the radio emission, generated by longer-lived particles, shows no particular increase in this central region. This indicates, somewhat surprisingly, that N206 is both a “composite” SNR, containing a PWN and shell structure together, and a “mixed morphology” SNR, with centrally concentrated X-ray emission that cannot be simply associated with the PWN. Indeed, N206 is not the only SNR to show this combination; for instance, the Galactic remnant W28 combines centrally concentrated X-ray emission with a probable off-center PWN (Rho & Borkowski 2002; Kassim 1992). Other examples include W44 (Cox et al. 1999; Rho et al. 1994; Harrus, Hughes, & Helfand 1996) and IC443 (Kawasaki et al. 2002; Bocchino & Bykov 2001; Olbert et al. 2001; Petre et al. 1988). We shall call this category “mixed-composite” SNRs, reflecting the combined action of separate physical processes influencing their emission.

The authors thank the anonymous referee for a very detailed critique of this work, which has much improved it, and also thank Brian D. Fields for valuable discussions. RMW and YHC acknowledge support from STSCI grant STI GO-08110. RMW, YHC, and JRD acknowledge support from NASA grant NAG 5-11159. RMW, YHC, FDS and JRD acknowledge support from SAO grant G03-4096. MAG acknowledges support from the grant AYA 2002-00376 of the Spanish MCyT (cofunded by FEDER funds).

REFERENCES

- Behar, E., Rasmussen, A. P., Griffiths, R. G., Dennerl, K., Audard, M., Aschenbach, B., & Brinkman, A. C. 2001, *A&AL*, 365, 242
- Bocchino, F. & Bykov, A. M. 2001, *A&A*, 376, 248
- Camilo, F. et al. 2002, *ApJL*, 567, 71
- Camilo, F. et al. 2002, *ApJL*, 595, 25
- Chevalier, R. A., & Liang, E. P. 1989, *ApJ*, 344, 332
- Chu, Y.-H., & Kennicutt, R. C. 1988, *AJ*, 95, 1111
- Cox, D., Shelton, S., Maciejewski, W., Smith, R. C., Plewa, T., Pawl, A., & Różyczka, M. 1999, *ApJ*, 524, 179
- Dunne, B., Chu, Y.-H., & Staveland-Smith, L. 2005, in preparation
- Fan, G. L. 2002, PhD Thesis, The University of Hong Kong
- Gaensler, B., van der Swaluw, E., Camilo, F., Kaspi, V. M., Baganoff, F. K., Yusef-Zadeh, F., & Manchester, R. N. 2004, *ApJ*, submitted, astro-ph/0312362
- Harrus, I. M., Hughes, J. P., & Helfand, D. J. 1996, *ApJL*, 464, 161
- Henize, K. G. 1956, *ApJS*, 2, 315
- Kassim, N. E. 1992, *AJ*, 103, 943
- Kawasaki, M. T. et al. 2002, *ApJ*, 572, 897
- Klinger, R. J., Dickel, J. R., Fields, B. D., & Milne, D. K. 2002, *AJ*, 124, 2135
- Mathewson, D. S. & Clarke, J. N. 1973, *ApJ*, 180, 725
- McDowell, J. C. 1994, Einstein Obs. Unscreened IPC Data Archive, SAO HEAD CD-ROM Series I
- Milne, D. K., Caswell, J. L., & Haynes, R. F. 1980, *MNRAS*, 191, 469
- Olbert, C. M., Clearfield, C. R., Williams, N. E., Keohane, J. W., & Frail, D. A. 2001, *ApJL*, 554, 205O

- Osterbrock, D. E., Fulbright, J. P., Martel, A. R., Keane, M. J., Trager, S. C., & Basri, G. 1996, *PASP*, 108, 277
- Park, S., Hughes, J. P., Burrows, D. N., Slane, P. O., Nousek, J. A., & Garmire, G. P. 2003, *ApJL*, 598, 95
- Petre, R., Szymkowiak, A. E., Seward, F. D., & Willingale, R. 1988, *ApJ*, 335, 215
- Rho, J., & Borkowski, K. J. 2002, *ApJ*, 575, 201
- Rho, J. & Petre, R. 1998, *ApJL*, 503, 167
- Rho, J., Petre, R., Schlegel, E. M., & Hester, J. J. 1994, *ApJ*, 430, 757
- Rohlfs, K., Kreitschmann, J., Feitzinger, J. V. & Siegman, B. C. 1984, *A&A*, 137, 343
- Russel, S. C. & Dopita, M. A. 1992, *ApJ*, 384, 508
- Sedov, L. I. 1959, *Similarity and Dimensional Methods in Mechanics* (New York: Academic)
- Smith, R. C. & MCELS Team 1999, *PASA*, 15, 163
- Trushkin, S., Verkhodanov, O. V., Chernenkov, V. N., & Andernach, H. 2000, *Baltic Astron.*, 9, 608
- Tsujimoto, T., Nomoto, K., Yoshii, Y., Hashimoto, M., Yanagida, S., & Thielemann, F.-K. 1995, *MNRAS*, 277, 945
- van der Swaluw, E. 2004, *AdSpR*, 33, 475
- van der Swaluw, E., Achterberg, A., Gallant, Y. A., Downes, T. P., & Keppens, R. 1998, *A&A*, 397, 913
- Wang, Q. D., Gotthelf, E. V., Chu, Y.-H. & Dickel, J. R. 2001, *ApJ*, 559, 275
- Williams, R. M., Chu, Y.-H., Dickel, J. R., Petre, R., Smith, R. C., & Tavarez, M. 1999, *ApJS*, 123, 467

Table 1. Optical Echelle Observations

Date	Line	Exposure	Position
2000 Dec 6	H α + N II	1200 s	E–W through “linear feature”
2000 Dec 6	H α + N II	1200 s	N–S through SNR center
2004 Jan 14	H α + N II	1200 s	E–W through bright filament

Table 2. X-ray Regions

Label	Name	ACIS cts	MOS cts	Hardness
Joint Chandra ACIS / XMM MOS regions				
1	Whole SNR	19,950	10,920	−0.49
2	Outer Limb	7,450	4,130	−0.45
3	Central	6,350	3,320	−0.58
4	Wedge	2,375	1,400	−0.46
5	Linear Feature	1350	430	−0.24
Small spatial regions (Chandra ACIS only)				
6	Knot	456	...	0.26
7	22'' W of knot	301	...	−0.35
8	44'' W of knot	264	...	−0.43
9	Point Src	94	...	0.50
10	Bow Shock	754	...	−0.45
11	Trail	196	...	0.076

Note. — Background-subtracted source counts. “Hardness” refers to the hardness ratio derived from Chandra ACIS counts. The “Hard” band is defined as 1.0–8.0 keV, the “Soft” band as 0.3–1.0 keV; the hardness ratio is $H-S/H+S$.

Table 3. Fits to X-ray emission for N206 SNR

Spectral Model	N_{H} cm^{-2}	kT keV	abundance frac. solar	τ $\text{cm}^{-3} \text{ s}$	norm cm^{-5}	χ^2 reduced	dof
Outer Limb Region (excludes “linear feature”)							
Merged ACIS							
pshock	$2.7_{-0.5}^{+1.1} \times 10^{21}$	$0.47_{-0.11}^{+0.04}$	$0.25_{-0.08}^{+0.03}$	$1.4_{-0.4}^{+0.9} \times 10^{11}$	$7 \pm 5 \times 10^{-4}$	1.38	154
mekal	$3.6_{-0.2}^{+0.8} \times 10^{21}$	$0.22_{-0.03}^{+0.01}$	$0.14_{-0.03}^{+0.09}$...	$6 \pm 2 \times 10^{-4}$	1.93	155
EPIC MOS1&2							
pshock	$7_{-3}^{+5} \times 10^{20}$	$0.50_{-0.08}^{+0.06}$	$0.20_{-0.06}^{+0.09}$	$3.4_{-1.0}^{+1.2} \times 10^{11}$	$8 \pm 2 \times 10^{-3}$	1.17	83
mekal	$2.3_{-0.4}^{+0.4} \times 10^{21}$	$0.24_{-0.01}^{+0.02}$	$0.08_{-0.02}^{+0.03}$...	0.1 ± 0.02	1.48	84
ACIS + EPIC MOS1&2							
pshock	$2.2_{-0.4}^{+0.5} \times 10^{21}$	$0.44_{-0.06}^{+0.04}$	$0.22_{-0.04}^{+0.04}$	$2.1_{-0.5}^{+0.6} \times 10^{11}$	$7 \pm 3 \times 10^{-4}$	1.54	241
mekal	$3.1_{-0.2}^{+0.3} \times 10^{21}$	$0.23_{-0.01}^{+0.01}$	$0.12_{-0.02}^{+0.05}$...	$1.5 \pm 0.3 \times 10^{-2}$ $6 \pm 2 \times 10^{-3}$ 0.12 ± 0.03	1.96	242
Central Region (excludes “linear feature”)							
Merged ACIS							
pshock	$3.5 \pm 0.4 \times 10^{21}$	0.34 ± 0.08	0.25 ± 0.05	$4 \pm 2 \times 10^{11}$	$1.4 \pm 0.9 \times 10^{-3}$	3.09	91
mekal	$3.9 \pm 0.3 \times 10^{21}$	0.22 ± 0.08	0.4 ± 0.2	...	$3 \pm 2 \times 10^{-3}$	3.79	92
EPIC MOS1&2							
pshock	$2.0 \pm 0.4 \times 10^{21}$	0.38 ± 0.04	0.14 ± 0.03	$2.7 \pm 0.9 \times 10^{11}$	$2 \pm 1 \times 10^{-3}$	2.10	64
mekal	$2.7 \pm 0.3 \times 10^{21}$	0.22 ± 0.01	0.11 ± 0.02	...	$1.0 \pm 0.4 \times 10^{-2}$	2.98	65
ACIS + EPIC MOS1&2							
pshock	$2.9 \pm 0.3 \times 10^{21}$	0.37 ± 0.02	0.25 ± 0.03	$3.0 \pm 0.2 \times 10^{11}$	$9 \pm 4 \times 10^{-4}$ $2.1 \pm 0.9 \times 10^{-3}$	3.21	159
mekal	$3.6 \pm 0.2 \times 10^{21}$	0.22 ± 0.06	0.4 ± 0.1	...	$3 \pm 1 \times 10^{-4}$ $6 \pm 2 \times 10^{-3}$	3.97	160

Note. — All spectra cover the range between 0.3-10.0 keV.

Table 4. Fits to X-ray Emission for “Whole SNR” Region of the N206 SNR

Parameter	Model Fits			
	CIE	NEI	Combined NEI + powerlaw	
component	vmekal	vpshock	vpshock	powerlaw
N_{H} (cm^{-2})	$2.8_{-0.1}^{+0.1} \times 10^{21}$	$2.2_{-0.1}^{+0.1} \times 10^{21}$	$2.2_{-0.1}^{+0.1} \times 10^{21}$	
kT (keV)	$0.264_{-0.004}^{+0.002}$	$0.453_{-0.006}^{+0.005}$	$0.43_{-0.01}^{+0.01}$...
O/ O_{\odot}	$0.36_{-0.02}^{+0.02}$	$0.32_{-0.01}^{+0.02}$	$0.30_{-0.01}^{+0.01}$...
Ne/ Ne_{\odot}	$0.24_{-0.02}^{+0.03}$	$0.22_{-0.01}^{+0.02}$	$0.24_{-0.01}^{+0.01}$...
Mg/ Mg_{\odot}	$0.66_{-0.05}^{+0.06}$	$0.39_{-0.03}^{+0.04}$	$0.41_{-0.03}^{+0.04}$...
Si/ Si_{\odot}	$0.9_{-0.2}^{+0.2}$	$0.28_{-0.08}^{+0.07}$	$0.3_{-0.2}^{+0.1}$...
Fe/ Fe_{\odot}	$0.18_{-0.01}^{+0.01}$	$0.20_{-0.02}^{+0.01}$	$0.21_{-0.02}^{+0.02}$...
τ ($\text{cm}^{-3} \text{ s}$)	...	$3.5_{-0.2}^{+0.2} \times 10^{11}$	$3.3_{-0.2}^{+0.2} \times 10^{11}$...
Γ	$2.2_{-0.4}^{+0.3}$
ACIS norm (cm^{-5})	$5.25_{-0.07}^{+0.07} \times 10^{-3}$	$1.75_{-0.02}^{+0.03} \times 10^{-3}$	$1.76_{-0.02}^{+0.03} \times 10^{-3}$	$2.3_{-0.6}^{+0.5} \times 10^{-5}$
MOS norm (cm^{-5})	$1.05_{-0.02}^{+0.01} \times 10^{-2}$	$3.47_{-0.06}^{+0.06} \times 10^{-3}$	$3.59_{-0.06}^{+0.07} \times 10^{-3}$	$7_{-7}^{+1} \times 10^{-6}$
χ_{red}^2	2.73	2.23	2.15	
dof	294	294	292	

Note. — Results in Tables 4-8 are from simultaneous fits to ACIS and EPIC MOS data. All spectra cover the range between 0.3-8.0 keV.

Table 5. Fits to X-ray Emission for “Outer Limb” Region of the N206 SNR

Parameter	Model Fits			
	CIE	NEI	Combined NEI + powerlaw	
component	vmekal	vpshock	vpshock	powerlaw
N_{H} (cm^{-2})	$2.9_{-0.2}^{+0.1} \times 10^{21}$	$1.7_{-0.1}^{+0.1} \times 10^{21}$	$1.7_{-0.1}^{+0.1} \times 10^{21}$	
kT (keV)	$0.237_{-0.02}^{+0.03}$	$0.46_{-0.01}^{+0.02}$	$0.46_{-0.01}^{+0.01}$...
$\text{O}/\text{O}_{\odot}$	$0.25_{-0.02}^{+0.04}$	$0.22_{-0.02}^{+0.01}$	$0.22_{-0.04}^{+0.01}$...
$\text{Ne}/\text{Ne}_{\odot}$	$0.20_{-0.02}^{+0.03}$	$0.25_{-0.03}^{+0.03}$	$0.25_{-0.03}^{+0.02}$...
$\text{Mg}/\text{Mg}_{\odot}$	$0.7_{-0.1}^{+0.1}$	$0.43_{-0.06}^{+0.06}$	$0.43_{-0.06}^{+0.07}$...
$\text{Si}/\text{Si}_{\odot}$	$0.8_{-0.3}^{+0.4}$	$0.2_{-0.1}^{+0.2}$	$0.2_{-0.1}^{+0.2}$...
$\text{Fe}/\text{Fe}_{\odot}$	$0.21_{-0.3}^{+0.2}$	$0.24_{-0.02}^{+0.02}$	$0.24_{-0.02}^{+0.02}$...
τ ($\text{cm}^{-3} \text{ s}$)	...	$2.2_{-0.2}^{+0.2} \times 10^{11}$	$2.2_{-0.2}^{+0.2} \times 10^{11}$...
Γ	2_{-2}^{+3}
ACIS norm (cm^{-5})	$2.69_{-0.06}^{+0.05} \times 10^{-3}$	$5.1_{-0.1}^{+0.1} \times 10^{-4}$	$5.0_{-0.1}^{+0.2} \times 10^{-4}$	$2_{-2}^{+4} \times 10^{-6}$
MOS norm (cm^{-5})	$5.8_{-0.1}^{+0.2} \times 10^{-2}$	$1.11_{-0.04}^{+0.02} \times 10^{-2}$	$1.11_{-0.04}^{+0.03} \times 10^{-2}$	$0_{-0}^{+2 \times 10^{-5}}$
χ_{red}^2	1.71	1.47	1.48	
dof	203	203	201	

Table 6. Fits to X-ray Emission for “Central” Region of the N206 SNR

Parameter	Model Fits			
	CIE	NEI	Combined NEI + powerlaw	
component	vmekal	vpshock	vpshock	powerlaw
N_{H} (cm^{-2})	$2.8^{+0.01}_{-0.02} \times 10^{21}$	$3.0^{+0.1}_{-0.1} \times 10^{21}$	$2.7^{+0.1}_{-0.2} \times 10^{21}$	
kT (keV)	$0.278^{+0.002}_{-0.003}$	$0.335^{+0.002}_{-0.006}$	$0.37^{+0.02}_{-0.01}$...
O/ O_{\odot}	$0.56^{+0.05}_{-0.04}$	$0.46^{+0.02}_{-0.04}$	$0.46^{+0.04}_{-0.02}$...
Ne/ Ne_{\odot}	$0.16^{+0.07}_{-0.03}$	$0.24^{+0.03}_{-0.02}$	$0.27^{+0.04}_{-0.02}$...
Mg/ Mg_{\odot}	$0.9^{+0.1}_{-0.1}$	$0.5^{+0.2}_{-0.1}$	$0.6^{+0.1}_{-0.1}$...
Si/ Si_{\odot}	$0.7^{+0.2}_{-0.3}$	$0.3^{+0.2}_{-0.2}$	$0.3^{+0.2}_{-0.2}$...
Fe/ Fe_{\odot}	$0.22^{+0.01}_{-0.04}$	$0.21^{+0.02}_{-0.03}$	$0.23^{+0.02}_{-0.02}$...
τ ($\text{cm}^{-3} \text{ s}$)	...	$9^{+1}_{-1} \times 10^{11}$	$5.5^{+1}_{-1} \times 10^{11}$...
Γ	3^{+3}_{-3}
ACIS norm (cm^{-5})	$1.22^{+0.03}_{-0.03} \times 10^{-3}$	$1.13^{+0.02}_{-0.03} \times 10^{-3}$	$7.7^{+0.2}_{-0.3} \times 10^{-4}$	$2^{+0.3}_{-0.3} \times 10^{-6}$
MOS norm (cm^{-5})	$2.72^{+0.08}_{-0.08} \times 10^{-3}$	$2.5^{+0.1}_{-0.1} \times 10^{-3}$	$1.7^{+0.1}_{-0.1} \times 10^{-3}$	$0^{+3 \times 10^{-6}}_{-0}$
χ^2_{red}	2.50	2.22	2.18	
dof	150	150	148	

Table 7. Fits to X-ray Emission for “Wedge” Region of the N206 SNR

Parameter	Model Fits			
	CIE	NEI	Combined NEI + powerlaw	
component	vmekal	vpshock	vpshock	powerlaw
N_{H} (cm^{-2})	$2.3_{-0.2}^{+0.2} \times 10^{21}$	$2.2_{-0.1}^{+0.1} \times 10^{21}$	$1.8_{-0.1}^{+0.1} \times 10^{21}$	
kT (keV)	$0.32_{-0.01}^{+0.01}$	$0.90_{-0.05}^{+0.04}$	$0.66_{-0.02}^{+0.03}$...
O/ O_{\odot}	$0.31_{-0.04}^{+0.04}$	$0.30_{-0.03}^{+0.03}$	$0.39_{-0.03}^{+0.04}$...
Ne/ Ne_{\odot}	$0.09_{-0.03}^{+0.02}$	$0.12_{-0.04}^{+0.04}$	$0.14_{-0.04}^{+0.06}$...
Mg/ Mg_{\odot}	$0.36_{-0.09}^{+0.08}$	$0.2_{-0.2}^{+0.1}$	$0.4_{-0.1}^{+0.1}$...
Si/ Si_{\odot}	$0.8_{-0.3}^{+0.2}$	$0.2_{-0.1}^{+0.2}$	$0.1_{-0.1}^{+0.2}$...
Fe/ Fe_{\odot}	$0.06_{-0.02}^{+0.01}$	$0.19_{-0.03}^{+0.02}$	$0.19_{-0.04}^{+0.02}$...
τ (cm^{-3} s)	...	$7_{-1}^{+1} \times 10^{10}$	$2.1_{-0.3}^{+0.1} \times 10^{11}$...
Γ	$1.6_{-0.9}^{+0.9}$
ACIS norm (cm^{-5})	$5.9_{-0.02}^{+0.02} \times 10^{-4}$	$1.05_{-0.05}^{+0.03} \times 10^{-4}$	$1.14_{-0.03}^{+0.05} \times 10^{-4}$	$2_{-1}^{+2} \times 10^{-6}$
MOS norm (cm^{-5})	$4.3_{-0.2}^{+0.2} \times 10^{-2}$	$7.5_{-0.4}^{+0.3} \times 10^{-3}$	$7.9_{-0.4}^{+0.4} \times 10^{-4}$	$2.3_{-0.9}^{+0.8} \times 10^{-4}$
χ_{red}^2	1.49	1.07	0.98	
dof	102	102	100	

Table 8. Fits to X-ray Emission for “Linear Feature” Region of the N206 SNR

Parameter	Model Fits				
	CIE	NEI	Combined NEI + powerlaw		powerlaw
component	vmekal	vpshock	vpshock	powerlaw	powerlaw
N_{H} (cm^{-2})	$1.0^{+0.4}_{-0.3} \times 10^{21}$	$3.5^{+0.4}_{-0.5} \times 10^{21}$	$2.2^{+0.5}_{-0.4} \times 10^{21}$		$2.6^{+0.7}_{-0.7} \times 10^{21}$
kT (keV)	$2.0^{+0.5}_{-0.3}$	$2.8^{+0.9}_{-0.6}$	$0.4^{+0.2}_{-0.1}$
O/ O_{\odot}	2^{+3}_{-2}	$0.15^{+0.06}_{-0.08}$	$0.2^{+0.4}_{-0.2}$
Ne/ Ne_{\odot}	2^{+2}_{-2}	$0.18^{+0.07}_{-0.09}$	$0.2^{+0.5}_{-0.2}$
Mg/ Mg_{\odot}	1^{+2}_{-1}	$0.3^{+0.2}_{-0.1}$	$0.7^{+0.5}_{-0.5}$
Si/ Si_{\odot}	$0.1^{+0.5}_{-0.1}$	$0.2^{+0.3}_{-0.2}$	$0.4^{+0.9}_{-0.4}$
Fe/ Fe_{\odot}	$0.1^{+0}_{-0.1}$	$0.11^{+0.05}_{-0.05}$	$0.1^{+0.1}_{-0.1}$
τ ($\text{cm}^{-3} \text{ s}$)	...	$4^{+1}_{-2} \times 10^{10}$	$5 \times 10^{13\text{a}}$
Γ	$2.2^{+0.3}_{-0.3}$	$2.8^{+0.2}_{-0.3}$
ACIS norm	$4.5^{+0.4}_{-0.5} \times 10^{-4}$	$4.2^{+0.4}_{-0.5} \times 10^{-5}$	$3^{+2}_{-2} \times 10^{-5}$	$1.5^{+0.1}_{-0.3} \times 10^{-5}$	$2.4^{+0.7}_{-0.6} \times 10^{-5}$
MOS norm	$1.1^{+0.1}_{-0.2} \times 10^{-4}$	$1.0^{+0.2}_{-0.1} \times 10^{-4}$	$2.0^{+0.5}_{-0.3} \times 10^{-4}$	$2.7^{+0.5}_{-0.7} \times 10^{-5}$	$6^{+1}_{-2} \times 10^{-5}$
χ^2_{red}	1.13	1.04	0.93		1.08
dof	92	92	90		92

^aError estimation gave a range of 6×10^{12} to $5 \times 10^{13} \text{ cm}^{-3} \text{ s}$; the latter is the hard limit for this parameter. At this upper limit the plasma is considered to be in ionization equilibrium.

Table 9. Small-region fits (Chandra ACIS only)

Region	kT	τ	Γ	K_{pshock}	K_{pow}	χ^2/dof
Knot	$0.9_{-0.5}^{+0.8}$	$4_{-9}^{+8} \times 10^{10}$	$1.7_{-0.2}^{+0.2}$	$2.6_{-0.9}^{+0.6} \times 10^{-6}$	$7_{-1}^{+1} \times 10^{-6}$	0.89/18
22'' W of knot	$2.0_{-0.7}^{+0.8}$	$3_{-1}^{+1} \times 10^{10}$	2_{-1}^{+1}	$7_{-1}^{+1} \times 10^{-6}$	$1.2_{-0.7}^{+0.7} \times 10^{-6}$	0.67/15
44'' W of knot	$0.36_{-0.04}^{+0.05}$	$8_{-4}^{+8} \times 10^{11}$	3_{-1}^{+1}	$2.4_{-0.4}^{+0.3} \times 10^{-5}$	$1.8_{-0.9}^{+0.8} \times 10^{-6}$	0.78/15
Point Source	$2.1_{-0.5}^{+0.4}$...	$2.4_{-0.5}^{+0.4} \times 10^{-6}$	1.4/6

Note. — All spectra cover the range between 0.3-8.0 keV. For these fits, combined NEI plasma (pshock) and power-law (pow) models were used. N_H was fixed at a value of $2.2 \times 10^{21} \text{ cm}^{-2}$ and abundances were set to 30% solar, consistent with similar fits for this area above.

Table 10. Derived Physical Parameters for SNR N206

Region		
Cool shell	density	$10 \pm 4 \text{ cm}^{-3}$
Cool shell	mass	$160 - 2000 M_{\odot}$
Cool shell	expansion velocity	$202 \pm 5 \text{ km s}^{-1}$
Cool shell	kinetic energy	$1 - 8 \times 10^{50} \text{ erg}$
Cool shell	thermal pressure	$3 \pm 1 \times 10^{-11} \text{ dyne cm}^{-2}$
Hot gas	temperature	$0.4 \pm 0.1 \text{ keV}$
Hot gas	density	$0.24 f_{hot}^{-1/2} \text{ cm}^{-3}$
Hot gas	mass	$270 \pm 10 f_{hot}^{1/2} M_{\odot}$
Hot gas	thermal energy	$6 \pm 1 \times 10^{50} f_{hot}^{1/2} \text{ erg}$
Hot gas	thermal pressure	$3.3 \pm 0.4 \times 10^{-10} f_{hot}^{1/2} \text{ dyne cm}^{-2}$

Table 11. Linear Feature Thermal vs Nonthermal X-ray Emission (Chandra ACIS only)

Region	Power-Law Flux erg cm ⁻² s ⁻¹	Thermal Flux erg cm ⁻² s ⁻¹	Flux Ratio pwrlaw/thrml
By fitted spectral model components			
Knot	$2.2 \pm 0.6 \times 10^{-14}$	$2 \pm 1 \times 10^{-15}$	0.9/0.1
22" W of knot	$7 \pm 1 \times 10^{-15}$	$7.5 \pm 0.5 \times 10^{-15}$	0.5/0.5
44" W of knot	$2.7 \pm 0.4 \times 10^{-15}$	$7.9 \pm 0.7 \times 10^{-15}$	0.3/0.7
By energy range (Thermal: 0.3-1.0 keV; Powerlaw: 2.0-8.0 keV)			
Knot	$2.3 \pm 0.2 \times 10^{-14}$	$4.3 \pm 0.3 \times 10^{-15}$	0.8/0.2
22" W of knot	$8.3 \pm 0.1 \times 10^{-15}$	$7.3 \pm 0.2 \times 10^{-15}$	0.5/0.5
44" W of knot	$8 \pm 1 \times 10^{-16}$	$7.3 \pm 0.1 \times 10^{-15}$	0.1/0.9

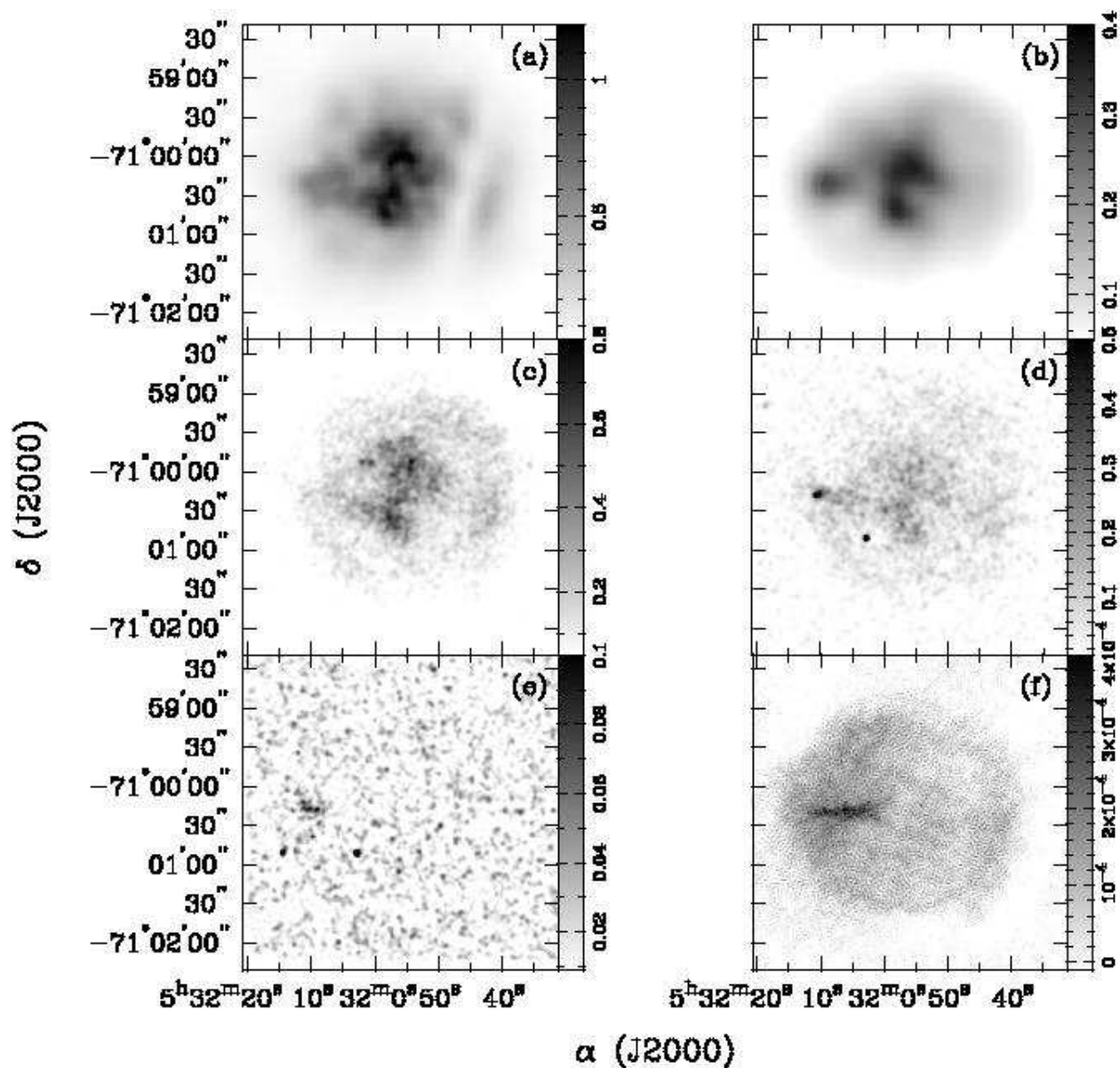


Fig. 1.— Smoothed images, over the same spatial region: (a) *XMM-Newton* EPIC-pn 0.2-10.0 keV (b) *XMM-Newton* EPIC-MOS 0.2-10.0 keV (c) *Chandra* ACIS 0.2-0.9 keV (d) *Chandra* ACIS 0.9-3.0 keV (e) *Chandra* ACIS 3.0-8.0 keV (f) ATCA radio 6 cm. *XMM-Newton* images are adaptively smoothed with the same scaling map; *Chandra* images are smoothed with a Gaussian ($\sigma = 3$).

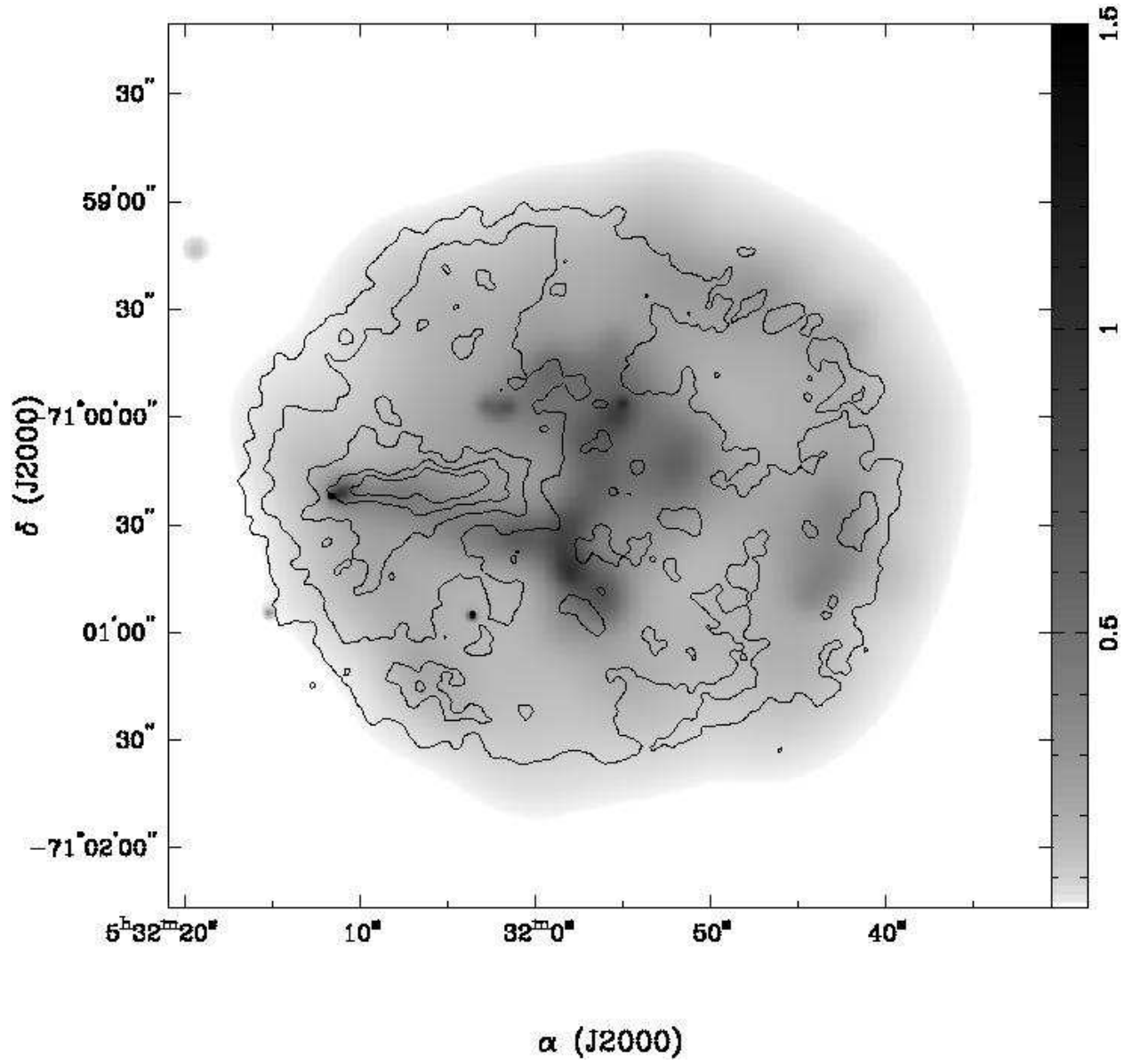


Fig. 2.— Adaptively smoothed Chandra ACIS 0.3-10.0 keV image (grayscale) with ATCA 6 cm radio contours overlaid.

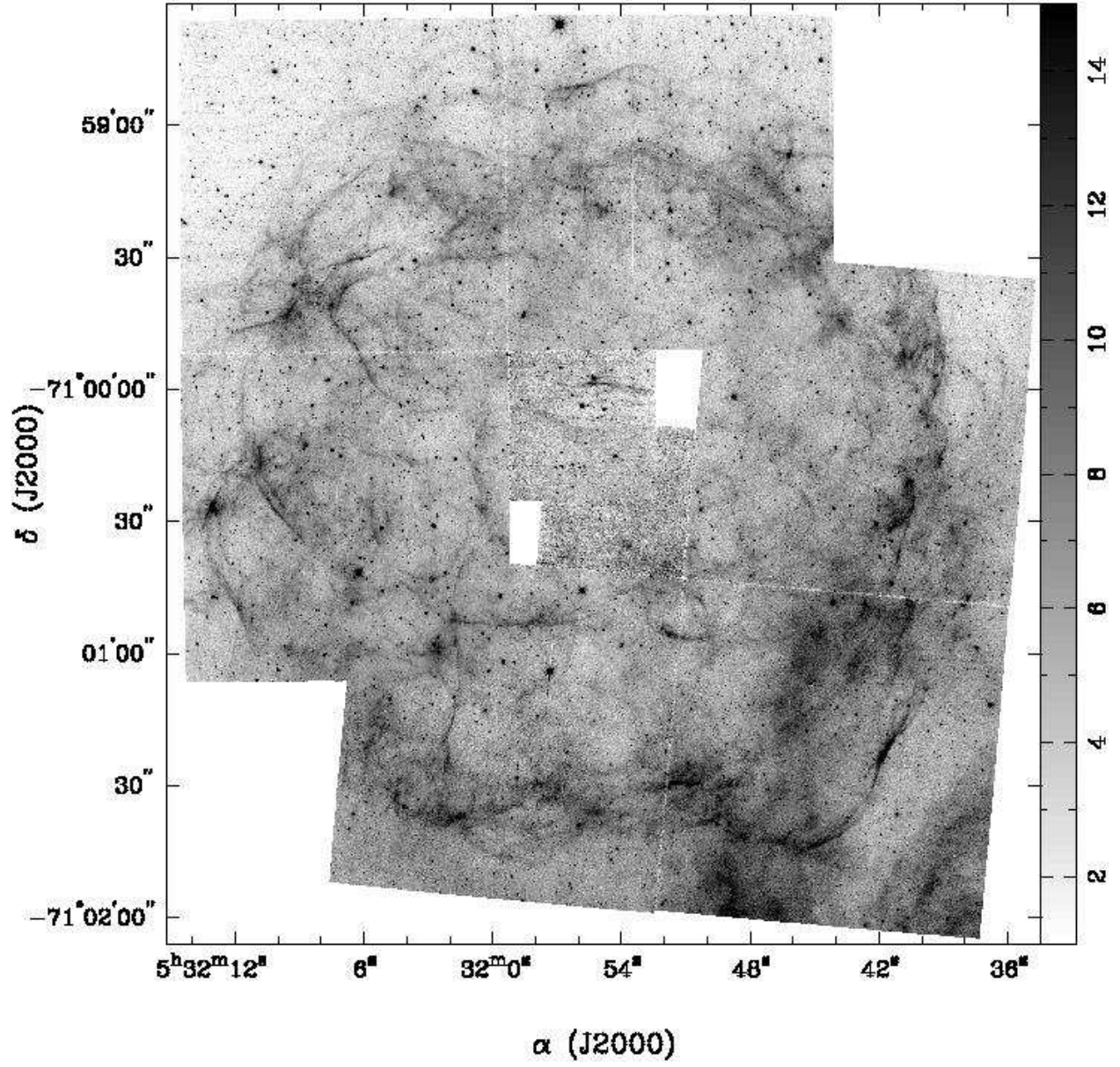


Fig. 3.— Combined HST WFPC2 mosaicked images of N206 in H α .

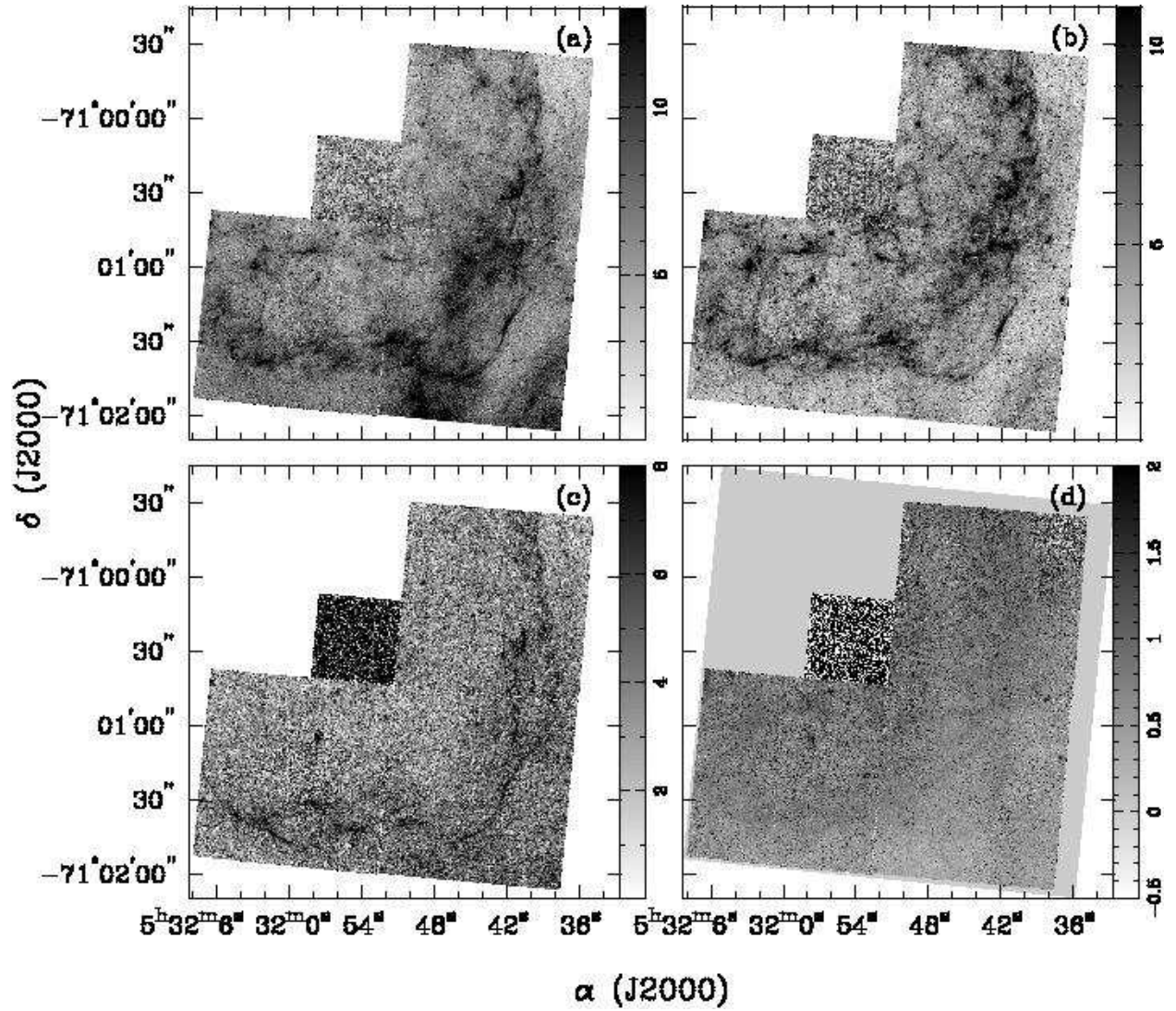


Fig. 4.— HST WFPC2 mosaicked images of the southwest side of N206 in (a) $\text{H}\alpha$, (b) $[\text{S II}]$, (c) $[\text{O III}]$ and (d) $[\text{S II}]/\text{H}\alpha$ ratio map.

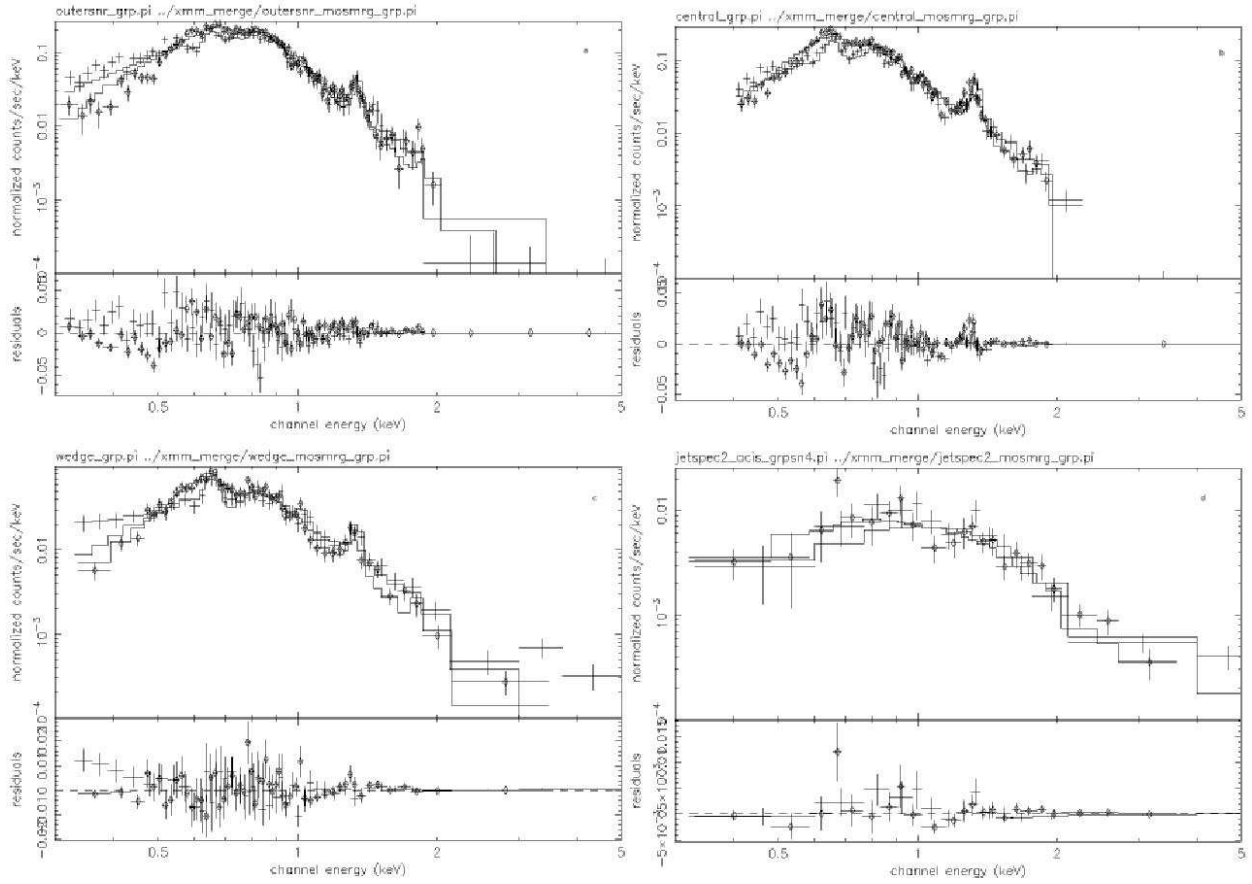


Fig. 5.— Chandra ACIS (crosses) and XMM-Newton EPIC-MOS (dotted crosses) spectra, fits and residuals for four extraction regions: (a) Region 2, outer limb; (b) Region 3, central; (c) Region 4, wedge; (d) Region 5, linear feature.

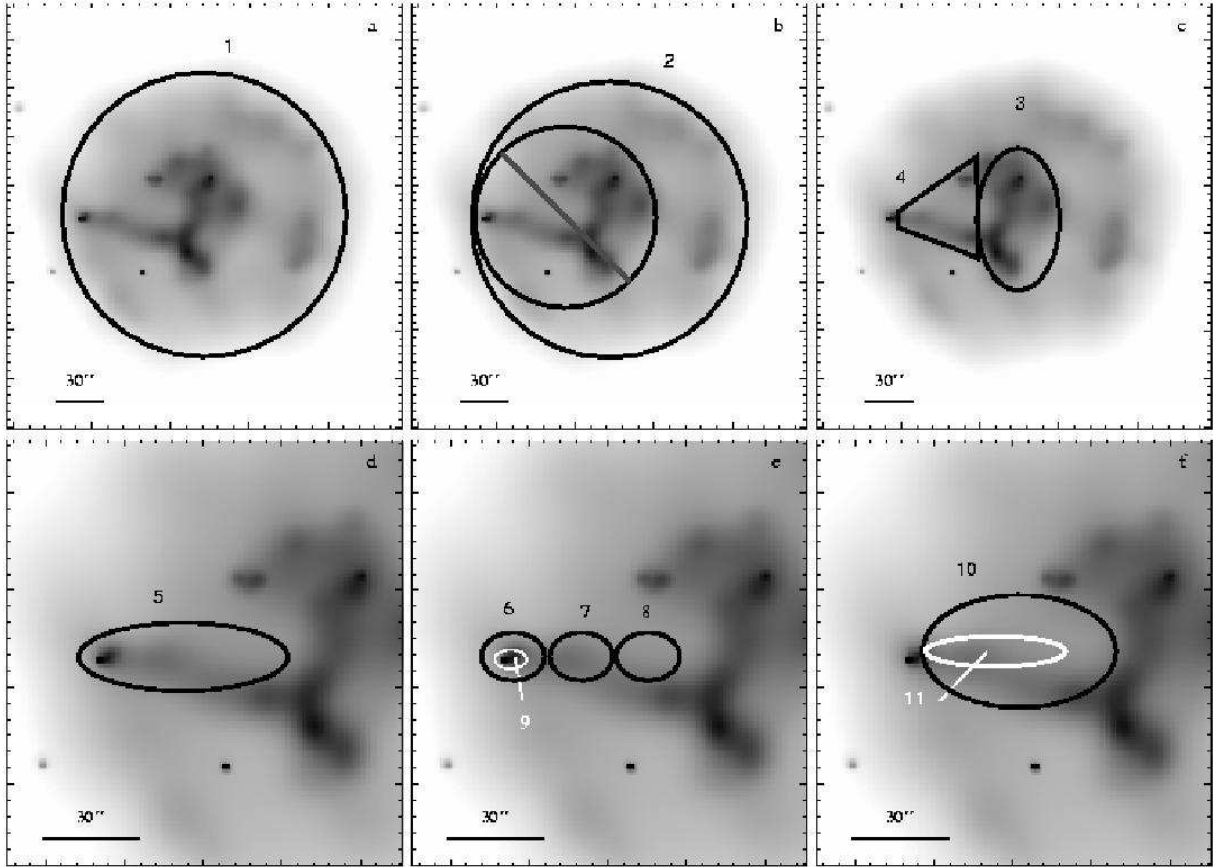


Fig. 6.— Smoothed Chandra ACIS image with regions for spectral analysis, as listed in Table 2, overlaid and labeled. (a) Region 1; (b) Region 2; (c) Regions 3-4; (d) Region 5; (e) Regions 6-9; (f) Regions 10-11.

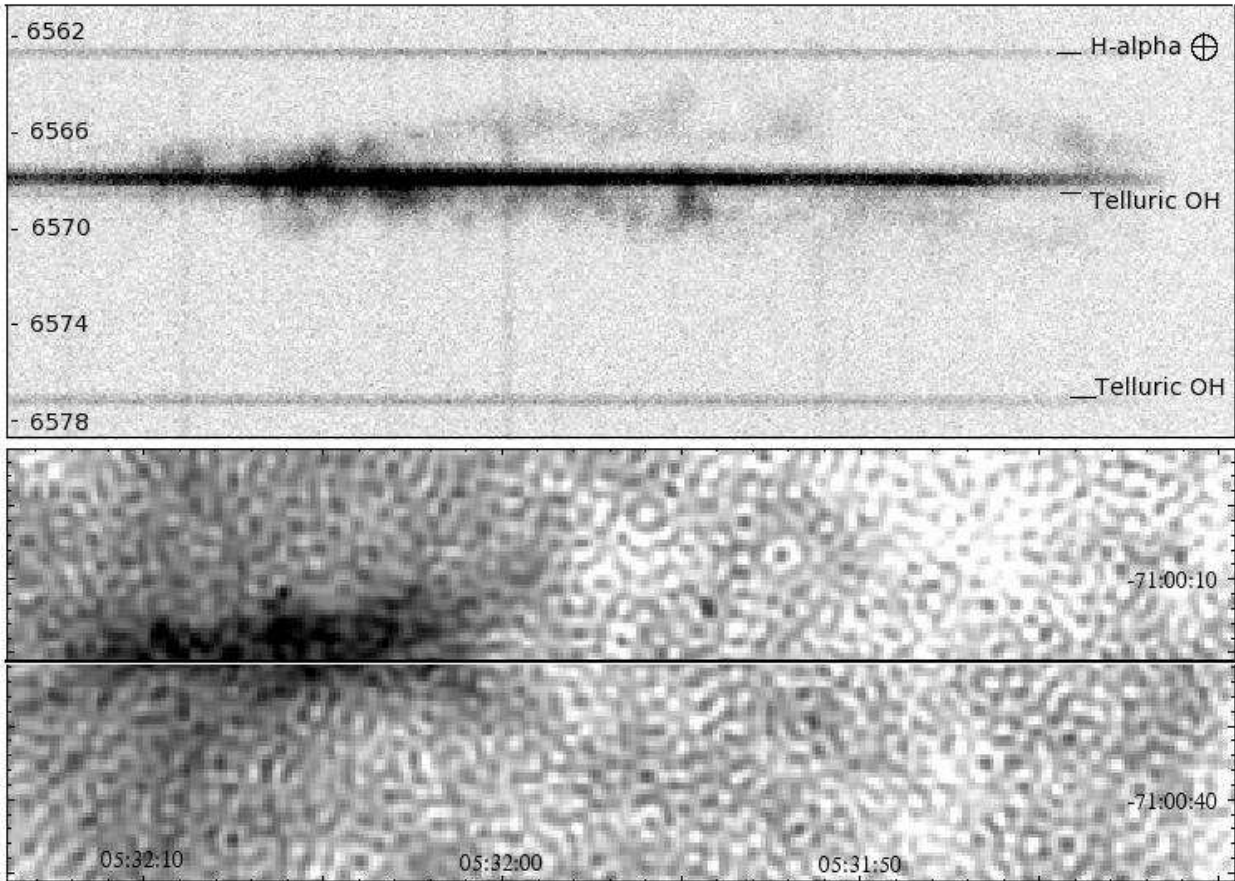


Fig. 7.— Top: echelle spectrum along “linear feature”. Bottom: ATCA 6 cm radio image of “linear feature” showing slit location.